

The peculiar motions of early-type galaxies in two distant regions – II. The spectroscopic data

Gary Wegner¹, Matthew Colless², R. P. Saglia³, Robert K. McMahan Jr^{4,5},
Roger L. Davies⁶, David Burstein⁷ and Glenn Baggle⁶

¹*Department of Physics and Astronomy, 6127 Wilder Laboratory, Dartmouth College, Hanover, NH 03755-3528, U.S.A.*

²*Mount Stromlo and Siding Spring Observatories, The Australian National University, Weston Creek, ACT 2611, Australia*

³*Universitäts-Sternwarte München, Scheinerstraße 1, D-81679 München, Germany*

⁴*Dept of Physics and Astronomy, University of North Carolina, CB 3255 Phillips Hall, Chapel Hill, NC 27599-3255, U.S.A.*

⁵*P.O. Box 14026, McMahan Research Laboratories, 79 Alexander Drive, Research Triangle, NC 27709, U.S.A.*

⁶*Department of Physics, South Road, Durham DH1 3LE, United Kingdom*

⁷*Department of Physics and Astronomy, Box 871054, Arizona State University, Tempe, AZ 85287-1504, U.S.A.*

Accepted —. Received —; in original form —.

ABSTRACT

We present the spectroscopic data for the galaxies studied in the EFAR project, which is designed to measure the properties and peculiar motions of early-type galaxies in two distant regions. We have obtained 1319 spectra of 714 early-type galaxies over 33 observing runs on 10 different telescopes. We describe the observations and data reductions used to measure redshifts, velocity dispersions and the Mgb and Mg₂ Lick linestrength indices. Detailed simulations and intercomparison of the large number of repeat observations lead to reliable error estimates for all quantities. The measurements from different observing runs are calibrated to a common zeropoint or scale before being combined, yielding a total of 706 redshifts, 676 velocity dispersions, 676 Mgb linestrengths and 582 Mg₂ linestrengths. The median estimated errors in the combined measurements are $\Delta cz=20 \text{ km s}^{-1}$, $\Delta\sigma/\sigma=9.1\%$, $\Delta\text{Mgb}/\text{Mgb}=7.2\%$ and $\Delta\text{Mg}_2=0.015 \text{ mag}$. Comparison of our measurements with published datasets shows no systematic errors in the redshifts or velocity dispersions and only small zeropoint corrections to bring our linestrengths onto the standard Lick system. We have assigned galaxies to physical clusters by examining the line-of-sight velocity distributions based on EFAR and ZCAT redshifts, together with the projected distributions on the sky. We derive mean redshifts and velocity dispersions for these clusters, which will be used in estimating distances and peculiar velocities and to test for trends in the galaxy population with cluster mass. The spectroscopic parameters presented here for 706 galaxies combine high quality data, uniform reduction and measurement procedures, and detailed error analysis. They form the largest single set of velocity dispersions and linestrengths for early-type galaxies published to date.

Key words: galaxies: clustering — galaxies: distances and redshifts — galaxies: elliptical and lenticular, cD — large scale structure of universe — surveys

1 INTRODUCTION

We are measuring the peculiar motions of galaxy clusters in the Hercules-Corona Borealis (HCB) and Perseus-Pisces-Cetus (PPC) regions at distances between 6000 and 15000 km s^{-1} using the global properties of elliptical galaxies. This study (the EFAR project) has as primary goals: (i) characterising the intrinsic properties of elliptical galaxies in clusters by compiling a large and homogeneous sample with high-quality photometric and spectroscopic data; (ii) testing possible systematic errors, such as environmen-

tal dependence, in existing elliptical galaxy distance estimators; (iii) deriving improved distance estimators based on a more comprehensive understanding of the properties of ellipticals and how these are affected by the cluster environment; and (iv) determining the peculiar velocity field in regions that are dynamically independent of the mass distribution within 5000 km s^{-1} of our Galaxy in order to test whether the large-amplitude coherent flows seen locally are typical of bulk motions in the universe.

The background and motivation of this work are dis-

cussed in Paper I of this series (Wegner et al. 1996), which also describes in detail the choice of regions to study, the sample of clusters and groups, and the selection procedure and selection functions of the programme galaxies. In earlier papers we reported the photoelectric photometry for 352 programme galaxies which underpins the transformation of our CCD data to the standard R magnitude system (Colless et al. 1993), and described our technique for correcting for the effects of seeing on our estimates of length scales and surface brightnesses (Saglia et al. 1993). This paper (Paper II) describes the spectroscopic observations and gives redshifts, velocity dispersions and linestrength indices for the programme galaxies. The CCD imaging observations of these galaxies, and their photometric parameters, are described in Paper III (Saglia et al. 1997), while descriptions of the profile fitting techniques used to determine these parameters (along with detailed simulations establishing the uncertainties and characterising the systematic errors) are given in Paper IV (Saglia et al. 1997). The Mg- σ relation and its implications are discussed in Paper V (Colless et al. 1998). Subsequent papers in the series will explore other intrinsic properties of the galaxies and their dependence on environment, derive an optimal distance estimator, and discuss the peculiar motions of the clusters in each of our survey regions and their significance for models of the large-scale structure of the universe.

The structure of the present paper is as follows. In §2 we describe the observations and reductions used in obtaining the 1319 spectra in our dataset (1250 spectra for 666 programme galaxies and 69 spectra for 48 calibration galaxies) and discuss the quality of the data. We explain the techniques by which redshifts, velocity dispersions and linestrength indices were estimated from the spectra in §3, including the various corrections applied to the raw values. In §4 we describe the method used to combine data from different runs and evaluate the internal precision of our results using the large number of repeat measurements in our dataset. We then give the final values of the spectroscopic parameters for each galaxy in our sample: we have redshifts for 706 galaxies, dispersions and Mg*b* linestrengths for 676 galaxies and Mg₂ linestrengths for 582 galaxies. We compare our results to previous studies in the literature to obtain external estimates of our random and systematic errors. In §5 we combine our redshifts with those from ZCAT in order to assign sample galaxies to physical clusters, and to estimate the mean redshifts and velocity dispersions of these clusters. Our conclusions are summarised in §6.

This paper presents the largest and most homogeneous sample of velocity dispersions and linestrengths for elliptical galaxies ever obtained. The precision of our measurements is sufficiently good to achieve the goal of measuring distances via the Fundamental Plane out to 15000 km s⁻¹.

2 OBSERVATIONS

The spectroscopic observations for the EFAR project were obtained over a period of seven years from 1986 to 1993 in a total of 33 observing runs on 10 different telescopes. In this section we describe the spectroscopic setups, the observing procedures, the quality of the spectra and the data-reduction

techniques. Further detail on these points is given by Baggeley (1996).

2.1 Spectroscopic Setups

Table 1 gives the spectroscopic setup for each run, including the run number, date, telescope, spectrograph and detector, wavelength range, spectral dispersion (in Å/pixel), effective resolution (in km s⁻¹), and the effective aperture size. Note that two runs (116 and 130) produced no useful data and are included in Table 1 only for completeness. Three runs utilised fibre spectrographs: runs 127 and 133 used Argus on the CTIO 4m and run 131 used MEFOS on the ESO 3.6m. All the other runs employed longslit spectrographs, mostly on 2m-class telescopes (MDM Hiltner 2.4m, Isaac Newton 2.5m, Kitt Peak 2.1m, Siding Spring 2.3m, Calar Alto 2.2m) although some 4m-class telescopes were also used (Kitt Peak 4m, William Herschel 4m, the MMT).

The spectra from almost all runs span at least the wavelength range 5126–5603Å, encompassing the Mg*b* 5174Å band and the FeI 5207Å and 5269Å features in the rest-frame for galaxies over the sample redshift range $cz \approx 6000$ –15000 km s⁻¹. The exceptions are the spectra from runs 115 and 131. Run 115 comprises 8 spectra obtained at the WHT with the blue channel of the ISIS spectrograph which have a red wavelength limit of 4970Å (i.e. including H β but not Mg*b*). Since we have spectra for all these galaxies from other runs we do *not* use the redshifts and dispersions from run 115. Run 131 comprises 128 spectra obtained at the ESO 3.6m with the MEFOS fibre spectrograph to a red limit of 5468Å, including Mg*b* and FeI 5207Å over the redshift range of interest, but not FeI 5269Å beyond $cz \approx 11000$ km s⁻¹. For most of the runs the spectra also encompass H β , and several span the whole range from CaI H+K 3933+3969Å to NaI D 5892Å.

The effective instrumental resolution of the spectra, σ_i , was measured from the autocorrelation of stellar template spectra (see §3.1 below), and ranged from 80 to 170 km s⁻¹, with a median value of 125 km s⁻¹. Both longslit and circular entrance apertures were used. Slits were typically 1.7–2.0 arcsec wide and the spectra were extracted to the point where the galaxy fell to about 10% of its peak value. Circular apertures (in the fibre spectrographs and the MMT Big Blue spectrograph) were between 1.9 and 2.6 arcsec in diameter. Further details of the observing setup for each telescope/instrument combination are given in Appendix A.

2.2 Observing Procedures

The total integration times on programme galaxies varied considerably depending on telescope aperture, observing conditions and the magnitude and surface brightness of the target (our programme galaxies have R band total magnitudes in the range 10–16). On 2m-class telescopes (with which the bulk of the spectroscopy was done), exposure times were usually in the range 30–60 min, with a median of 40 min; on 4m-class telescopes, exposure times were generally 15–20 min (up to 60 min for the faintest galaxies) with single-object slit spectrographs, but 60 or 120 min with the fibre spectrographs (where the aim was high S/N and completeness). Slit orientations were not generally aligned with

Table 1. The Spectroscopic Observing Runs

Run #	Date	Tele- ^a scope	Spectrograph + grating	Detector	$\lambda\lambda$ (Å)	$\Delta\lambda$ ^b (Å/pix)	σ_i ^c (km/s)	Aperture ^d (arcsec)	N^e
101	86/12	MG24	MarkIIIa+600B	GEC	4912–6219	2.27	145	1.9×10%	22
102	87/03	MG24	MarkIIIa+600B	RCA	4787–6360	3.10	145	1.9×10%	58
103	87/05	MG24	MarkIIIa+600B	RCA	4809–6364	3.07	145	1.9×10%	37
104	88/04	MG24	MarkIIIa+600V	RCA	5025–6500	2.90	125	1.9×10%	12
105	88/06	MG24	MarkIIIa+600V	RCA	5055–6529	2.90	125	1.9×10%	37
106	88/09	MG24	MarkIIIa+600V	Thompson	5041–6303	2.21	130	1.9×10%	23
107	88/10	MG24	MarkIIIa+600V	RCA	5048–6522	2.90	130	1.9×10%	27
108	88/07	MMTB	BigBlue+300B	Reticon	3700–7200	1.14	135	2.5	10
109	88/11	KP4M	RC+UV-Fast+17B	TI2	4890–5738	1.07	100	2.0×3.9	104
110	88/11	KP2M	GoldCam+#240	TI5	4760–5879	1.52	105	2.0×3.9	72
111	88/11	MMTB	BigBlue+300B	Reticon	3890–7500	1.34	135	2.5	20
112	89/04	MG24	MarkIIIb+600V	RCA	5066–6534	2.91	130	1.7×10%	34
113	89/06	MG24	MarkIIIb+600V	TI4849	5126–6393	2.18	150	2.4×10%	23
114	89/06	MMTB	BigBlue+300B	Reticon	3890–7500	1.34	135	2.5	12
115	89/08	WHT4	ISIS-Blue+R600B	CCD-IPCS	4330–4970	0.45	95	2.0×3.9	8
116 ^f	89/10	MMTR	RedChannel+600B	TI	4750–5950	1.50	125	1.5×10%	7
117	89/10	MG24	MarkIIIb+600V	Thompson	5031–6300	2.21	130	1.7×10%	61
118	89/11	MG24	MarkIIIb+600V	RCA	5018–6499	2.89	170	1.7×10%	14
119	90/05	MMTR	RedChannel+600B	TI	4750–5950	1.50	125	1.5×10%	17
120	90/10	IN25	IDS+235mm+R632V	GEC6	4806–5606	1.46	100	1.9×7.2	40
121	91/05	IN25	IDS+235mm+R632V	GEC3	4806–5603	1.46	100	1.9×7.2	87
122	91/10	MG24	MarkIIIb+600V	Thompson	5018–6278	2.20	125	1.7×10%	43
123	91/11	IN25	IDS+235mm+R632V	GEC3	4806–5603	1.46	100	1.9×7.2	29
124	92/01	MG24	MarkIIIb+600V	Thompson	5038–6267	2.15	125	1.7×10%	35
125	92/06	MG24	MarkIIIb+600V	Loral	4358–7033	1.31	125	1.7×10%	57
126	92/06	CA22	B&C spec+#7	TEK6	4800–6150	1.40	100	5.0×4.2	39
127 ^g	92/09	CT4M	Argus+KPGL#3	Reticon II	3877–6493	2.19	145	1.9	199
128	93/05	MG24	MarkIIIb+600V	Loral	5090–7050	1.40	105	1.7×10%	24
129	93/06	MG24	MarkIIIb+600V	TEK	4358–6717	2.31	135	1.7×10%	3
130 ^f	93/06	SS23	DBS-blue+600B	PCA	5015–5555	0.80	85	2.0×10%	0
131 ^g	93/10	ES36	MEFOS+B&C+#26	TEK512CB	4850–5468	1.22	105	2.6	128
132	93/10	SS23	DBS-blue+600B	Loral	4820–5910	1.10	80	2.0×10%	14
133 ^g	93/10	CT4M	Argus+KPGL#3	Reticon II	3879–6485	2.19	145	1.9	193

^a Telescopes: MG24=MDM 2.4m; KP4M/KP2M=KPNO 4m/2m; WHT4=William Herschel 4m (LPO); IN25=Isaac Newton 2.5m (LPO); MMTB/MMTR=MMT (blue/red); CA22=Calar Alto 2.2m; CT4M=Cerro Tololo 4m; SS23=Siding Spring 2.3m; ES36=ESO 3.6m.

^b Spectral dispersion in Å/pixel.

^c Instrumental resolution (σ , not FWHM) in km s^{-1} , as determined from the cross-correlation analysis calibration curves (see §3.1).

^d The aperture over which the galaxy spectrum was extracted: diameter for circular apertures and fibres, width×length for rectangular slits (10% means the spectrum was extracted out to the point where the luminosity had fallen to 10% of its peak value).

^e The number of spectra taken in the run.

^f These runs produced no useful data.

^g These runs used fibre spectrographs.

galaxy axes. The nominal goal in all cases was to obtain around 500 photons/Å at Mgb, corresponding to a S/N per 100 km s^{-1} resolution element of about 30. In fact our spectra have a median of 370 photons/Å at Mgb, corresponding to a S/N per 100 km s^{-1} of 26 (see §2.4).

In each run several G8 to K5 giant stars with known heliocentric velocities were observed. These ‘velocity standard stars’ are used as spectral templates for determining redshifts and velocity dispersions. In observing these standards care was taken to ensure that the illumination across the slit was uniform, in order both to remove redshift zeropoint errors and to mimic the illumination produced by a galaxy, thereby minimising systematic errors in velocity dispersion estimates. This was achieved in various ways: by defocussing the telescope slightly, by moving the star back and forth across the slit several times, or by trailing it up and down the slit. Such procedures were not necessary for standards obtained with fibre spectrographs, as internal reflections in

the fibres ensure even illumination of the spectrograph for all sources. Very high S/N (typically $>10,000$ photons/Å) were obtained in order that the stellar templates did not contribute to the noise in the subsequent analysis.

The normal calibration exposures were also obtained: bias frames, flatfields (using continuum lamps internal to the spectrographs or illuminating the dome) and spectra of wavelength calibration lamps before and/or after each galaxy or star exposure. In general we did not make use of spectrophotometric standards as fluxed spectra were not necessary and we wished to minimise overheads as much as possible.

The calibration procedures were slightly different for the three large datasets taken using fibre-fed spectrographs at CTIO (runs 127 and 133) and ESO (run 131). Because of the need to calibrate the relative throughput of the fibres in order to perform sky subtraction, fibre observations always included several twilight sky flatfield exposures. Each

velocity standard star was observed through several fibres by moving the fibres sequentially to accept the starlight.

2.3 Reductions

The reductions of both the longslit and fibre observations followed standard procedures as implemented in the IRAF^{*}, MIDAS and Starlink Figaro software packages. We briefly summarise the main steps in the reduction of our longslit and fibre data below; further details can be found in Baggley (1996).

The first stage of the reductions, common to all observations, was to remove the CCD bias using a series of bias frames taken at the start or end of the night. These frames were median-filtered and the result, scaled to the mean level of the CCD overscan strip, was subtracted from each frame in order to remove both the spatial structure in the bias pedestal and temporal variations in its overall level. We also took long dark exposures to check for dark current, but in no case did it prove significant. Subsequent reductions differed somewhat for longslit and fibre observations.

For longslit data, the next step was the removal of pixel-to-pixel sensitivity variations in the CCD by dividing by a sensitivity map. This map was produced by median-filtering the flatfield exposures (of an internal calibration lamp or dome lamp) and dividing this by a smoothed version of itself (achieved by direct smoothing or 2D surface fitting) in order to remove illumination variations in the ‘flat’ field. If necessary (because of a long exposure time or a susceptible CCD), cosmic ray events were identified and interpolated over in the two-dimensional image using either algorithmic or manual methods (or both).

The transformation between wavelength and pixel position in longslit data was mapped using the emission lines in the comparison lamp spectra. The typical precision achieved in wavelength calibration, as indicated by the residuals of the fit to the calibration line positions, was $\lesssim 0.1$ pixel, corresponding to $0.1\text{--}0.3\text{\AA}$ or $5\text{--}15\text{ km s}^{-1}$, depending on the spectrograph setup (see Table 1). The spectra were then rebinned into equal intervals of $\log \lambda$ so that each pixel corresponded to a fixed velocity interval, $\Delta v \equiv c\Delta z = c(10^{\Delta \log \lambda} - 1)$, chosen to preserve the full velocity resolution of the data.

The final steps in obtaining longslit spectra are sky-subtraction and extraction. The sky level was measured from two or more regions along the slit sufficiently far from the target object to be uncontaminated by its light. To account for variations in transmission along the slit, the sky under the object was interpolated using a low-order curve fitted to the slit illumination profile. A galaxy spectrum was then extracted by summing along the profile, usually over the range where the object’s luminosity was greater than $\sim 10\%$ of its peak value, but sometimes over a fixed width in arcsec (see Table 1). Standard star spectra were simply summed over the range along the slit that they had been trailed or defocussed to cover.

^{*} IRAF is distributed by the National Optical Astronomy Observatories which is operated by the Association of Universities for Research in Astronomy, Inc. under contract with the National Science Foundation.

For the fibre runs the individual object and sky spectra were extracted first, using a centroid-following algorithm to map the position of the spectrum along the CCD. The extraction algorithm fitted the spatial profile of the fibre, in order to remove cosmic ray events and pixel defects, and then performed a weighted sum over this fit out to the points where the flux fell to $\sim 5\%$ of the peak value. Next, the dome-illumination flatfield spectra were median-combined and a sensitivity map for each fibre constructed by dividing each fibre’s flatfield spectrum by the average over all fibres and normalising the mean of the result to unity. The pixel-to-pixel variations in the CCD response were then removed by dividing all other spectra from that fibre by this sensitivity map. Wavelength calibration was accomplished using the extracted comparison lamp spectra, giving similar precision to the longslit calibrations, and the object spectra were rebinned to a $\log \lambda$ scale. Using the total counts through each fibre from the twilight sky flatfield to give the relative throughputs, the several sky spectra obtained in each fibre exposure were median-combined (after manually removing ‘sky’ fibres which were inadvertently placed on faint objects). The resulting high- S/N sky spectrum, suitably normalised to each fibre’s throughput, was then subtracted from each galaxy or standard star spectrum.

The final step in the reductions for both longslit and fibre data was to manually clean all the one-dimensional spectra of remaining cosmic ray events or residual sky lines (usually only the 5577\AA line) by linearly interpolating over affected wavelengths.

2.4 Spectrum Quality

We have two methods for characterising the quality of our spectra. One is a classification of the spectra into 5 quality classes, based on our experience in reducing and analysing such data. Classes A and B indicate that both the redshift and the velocity dispersion are reliable (with class A giving smaller errors than class B); class C spectra have reliable redshifts and marginally reliable dispersions; class D spectra have marginally reliable redshifts but unreliable dispersions; class E spectra have neither redshifts nor dispersions. The second method is based on the S/N ratio per 100 km s^{-1} bin, estimated approximately from the mean flux over the restframe wavelength range used to determine the redshifts and dispersions (see §3.1) under the assumption that the spectrum is shot-noise dominated. These two measures of spectral quality are complementary: the S/N estimate is objective but cannot take into account qualitative problems which are readily incorporated in the subjective classifications. Figure 1 shows example spectra covering a range of quality classes and instrumental resolutions.

Figure 2 shows the S/N distribution for the whole sample and for each quality class individually, and gives the total number of objects, the fraction of the sample and the median S/N in each class. For the whole sample, 39% of the spectra have $S/N > 30$, 70% have $S/N > 20$, and 96% have $S/N > 10$. The two quality measures are clearly correlated, in the sense that better-classed spectra tend to have higher S/N . However there is also considerable overlap in the S/N range spanned by the different classes. This overlap has various sources: (i) factors other than S/N which affect the quality of the redshift and dispersion estimates, notably the

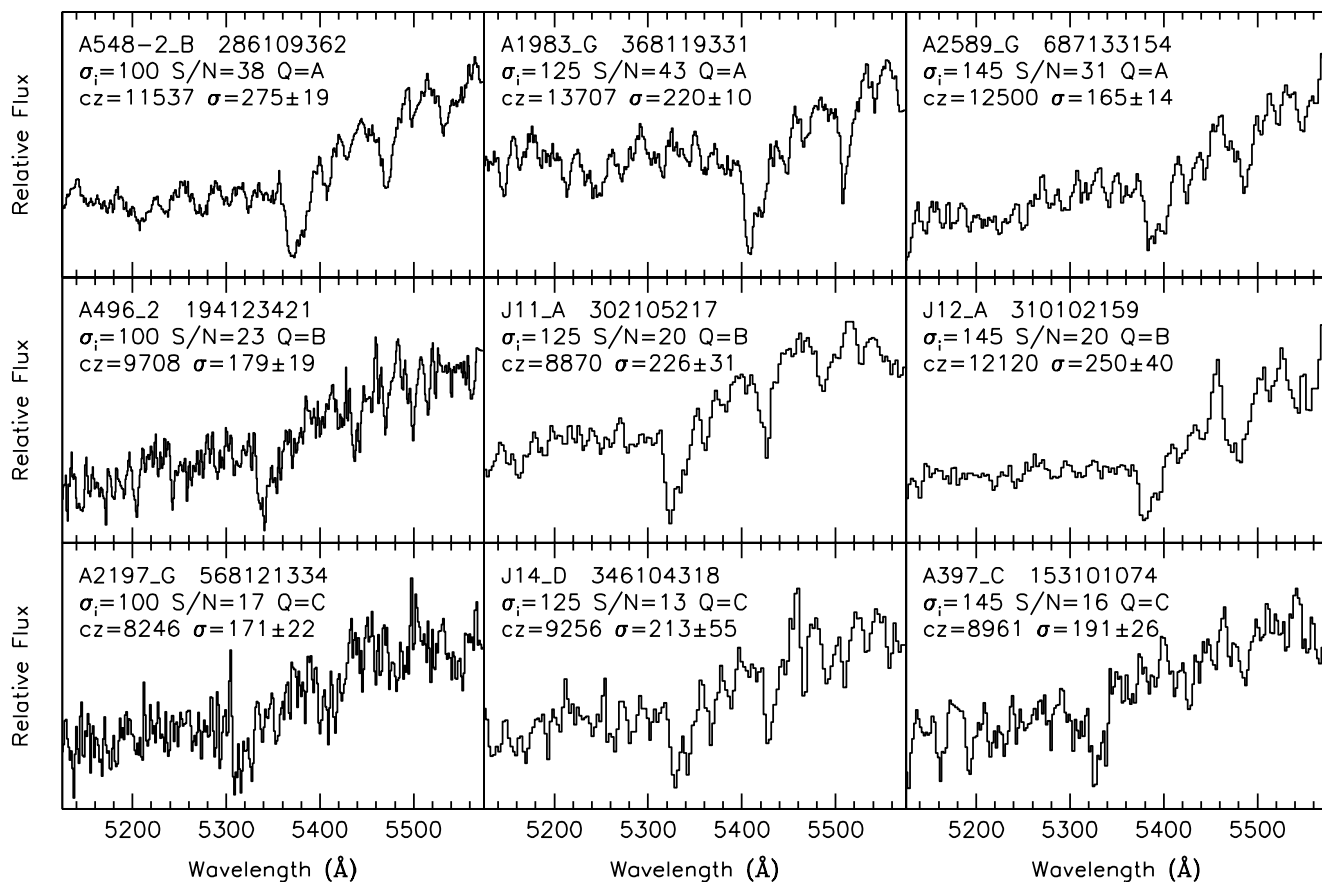


Figure 1. Example spectra covering a range of quality classes and instrumental resolutions: the top, middle and bottom rows are spectra with quality classes A, B and C respectively; the left, central and right columns are spectra with resolutions 100, 125 and 145 km s⁻¹ respectively. The label for each spectrum gives the galaxy name, the GINRUNSEQ spectrum identifier, the instrumental resolution, the S/N and quality class of the spectrum, the redshift, the dispersion and its estimated error. Note that the panels show relative flux and have a false zero for viewing convenience.

available restframe spectral range (which depends on both the spectrograph setup and the redshift of the target) and whether the object has emission lines; (ii) errors in estimating the S/N (e.g. due to sky subtraction errors, the neglect of the sky contribution in computing the S/N for fainter galaxies, or uncertainties in the CCD gain (affecting the conversion from counts to photons)); (iii) subjective uncertainties in the quality classification, particularly in determining the reliability of dispersion estimates (i.e. between classes B and C). Both ways of determining spectral quality are therefore needed in order to estimate the reliability and precision of the spectroscopic parameters we measure.

3 ANALYSIS

3.1 Redshifts and Dispersions

We derived redshifts and velocity dispersions from our spectra using the `fxcor` utility in IRAF, which is based on the cross-correlation method of Tonry & Davis (1979). We preferred this straightforward and robust method to more elaborate techniques since it is well-suited to the relatively modest S/N of our spectra. We used a two-step procedure, obtaining an initial estimate of the redshift using the whole

available spectrum and then using a fixed restframe wavelength range for the final estimates of redshift and velocity dispersion. The procedure was applied in a completely uniform manner to all the spectra in our sample as far as differences in wavelength range and resolution would allow.

The first step in the cross-correlation analysis is to fit and subtract the continuum of each spectrum in order to avoid the numerical difficulties associated with a dominant low-frequency spike in the Fourier transform. In the first pass through `fxcor` the continuum shape was fitted with a cubic spline with the number of segments along the spectrum chosen so that each segment corresponded to about 8000 km s⁻¹. Each iteration of the fit excluded points more than 1.5σ below or 3σ above the previous fit. In this way we achieved a good continuum fit without following broad spectral features. We then apodised 10% of the spectrum at each end with a cosine bell before padding the spectrum to 2048 pixels with zeros.

This continuum-subtracted, apodised spectrum was then Fourier transformed and a standard ‘ramp’ filter applied. This filter is described by 4 wavenumbers (k_1, k_2, k_3, k_4), rising linearly from 0 to 1 between k_1 and k_2 and then falling linearly from 1 to 0 between k_3 and k_4 . In the first pass these wavenumbers were chosen to be $k_1=4-$

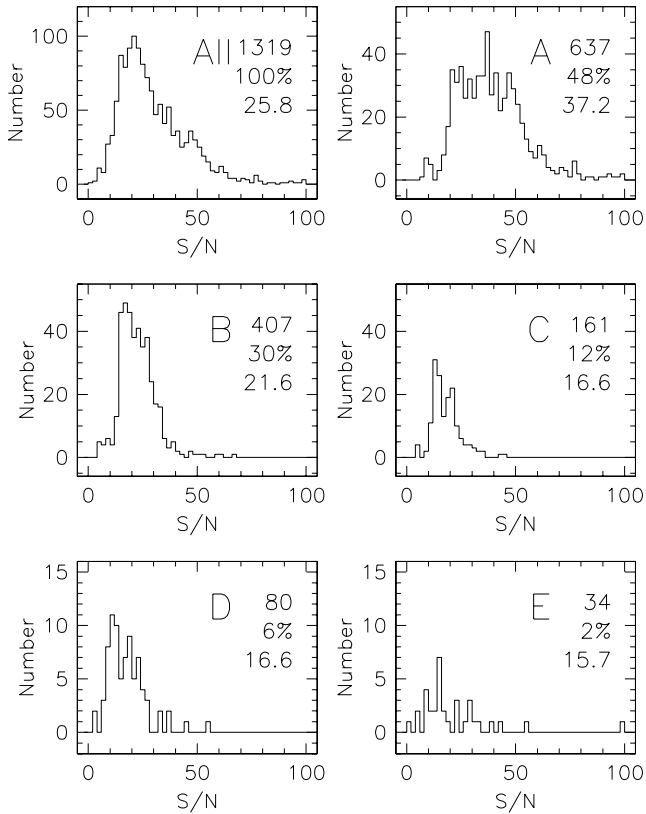


Figure 2. The distribution of S/N with quality class. For each class the panels give the total number of spectra, the percentage of the whole sample and the median S/N .

8 and $k_2=9-12$ (tailored to remove residual power from the continuum without affecting broad spectral features), and $k_3=N_{pix}/3$ and $k_4=N_{pix}/2$ (N_{pix} is the number of pixels in original spectrum before it is padded to 2048 pixels; these choices attenuate high-frequency noise and eliminate power beyond the Nyquist limit at $N_{pix}/2$). The same procedures were also applied to the spectrum of the stellar velocity standard to be used as a template. The cross-correlation of the galaxy and stellar template was then computed, and the top 90% of the highest cross-correlation peak fitted with a Gaussian in order to obtain a redshift estimate.

This procedure was repeated for every template from that run, and the redshifts corrected to the heliocentric frame. Offsets in the velocity zeropoint between templates, measured as the mean difference in the redshifts measured with different templates for all the galaxies in the run, were typically found to be $\lesssim 30 \text{ km s}^{-1}$. These were brought into relative agreement within each run by choosing the best-observed K0 template as defining the fiducial velocity zeropoint. Applying these offsets brought the galaxy redshifts estimated from different templates into agreement to within $\lesssim 3 \text{ km s}^{-1}$. (The removal of run-to-run velocity offsets is described below.) The mean over all templates then gave the initial redshift estimate for the galaxy.

This initial redshift was then used to determine the wavelength range corresponding to the restframe range $\lambda_{min}=4770\text{\AA}$ to $\lambda_{max}=5770\text{\AA}$. This range was chosen for use in the second pass through `fxcor` because: (i) it contains the MgI *b* 5174\AA band, H β 4861\AA and the FeI 5207\AA and 5269\AA

lines, but excludes the NaI D line at 5892\AA, which gives larger velocity dispersions than the lines in the region of Mg*b* (Faber & Jackson 1976); (ii) for redshifts up to our sample limit of $cz=15000 \text{ km s}^{-1}$ this restframe wavelength range is included in the great majority of our spectra. The input for the second pass was thus the available spectrum within the range corresponding to restframe 4770–5770\AA. All but two of our runs cover the restframe out to at least 5330\AA for $cz=15000 \text{ km s}^{-1}$; the exceptions are run 115 (which is not used for measuring dispersions) and run 131 (which reaches restframe 5207\AA).

In the second pass through `fxcor` we employed only minimal continuum subtraction based on a 1- or 2-segment cubic spline fit, preferring the better control over continuum suppression afforded by more stringent filtering at low wavenumbers. After considerable experimentation and simulation, we found that the best filter for recovering velocity dispersions was a ramp with the same k_3 and k_4 values as in the first pass, but with $k_2=0.01(N_{max} - N_{min})$, where N_{min} and N_{max} are the pixels corresponding to λ_{min} and λ_{max} , and $k_1=0.75k_2$. Again, the top 90% of the highest cross-correlation peak was fitted with a Gaussian. The position of this peak, corrected for the motion of the template star and the heliocentric motion of the earth relative to both the template and the galaxy, gave the final redshift estimate.

The galaxy’s velocity dispersion, σ_g , is in principle related to the dispersion of the Gaussian fitted to the cross-correlation peak, σ_x , by $\sigma_x^2 = \sigma_g^2 + 2\sigma_i^2$ (where σ_i is the instrumental resolution; Tonry & Davis 1979). In practice this relationship needs to be calibrated empirically because of the imperfect match between the spectra of a broadened stellar template and a galaxy and the effects of the filter applied to both spectra. The calibration relation between σ_x and σ_g for a typical case is shown in Figure 3 (see caption for more details). We estimate the instrumental resolution for a given run from the mean value of the calibration curve intercepts for all the templates in the run ($\sigma_i \approx \sigma_x/\sqrt{2}$ when $\sigma_g=0$); these are the values listed in Table 1.

The values of heliocentric radial velocity and velocity dispersion were determined in this second pass through `fxcor` for each galaxy spectrum using all the templates in the same run. The final step is then to combine the redshift and dispersion estimates from each template, as summarised below.

For the redshifts the steps involved were as follows: (i) Cases where the ratio of cross-correlation function peak height to noise (the R parameter defined by Tonry & Davis 1979) was less than 2 were rejected, as were cases that differed from the median by more than a few hundred km s^{-1} . (ii) The mean offset between the redshifts from a fiducial K0 template and each other template was used to shift all the redshifts from the other template to the velocity zeropoint of the fiducial. These offsets were typically $\lesssim 50 \text{ km s}^{-1}$. (iii) A mean redshift for each galaxy was then computed from all the unrejected cases using 2-pass 2σ clipping. (iv) Any template which gave consistently discrepant results was rejected and the entire procedure repeated. The scatter in the redshift estimates from different templates after this procedure was typically a few km s^{-1} .

A very similar procedure was followed in combining velocity dispersions except that a scale factor rather than an offset was applied between templates: (i) Cases with $R < 4$

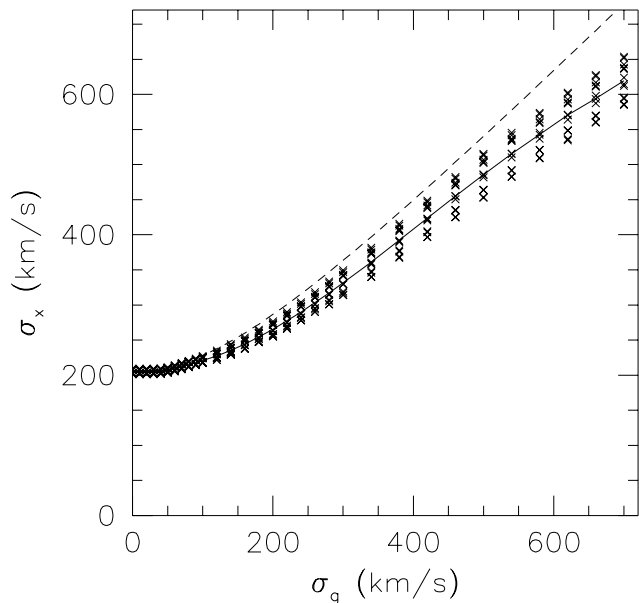


Figure 3. A typical calibration curve showing the relation between the width of the cross-correlation peak, σ_x , and the true velocity dispersion of the galaxy, σ_g . The crosses are the individual calibrations obtained by broadening each of the other templates in the run and cross-correlating with the template being calibrated. The solid curve is the calibration curve used, a series of linear segments joining the median value of σ_x at each calibrated value of σ_g . The dashed curve is the theoretical relation when no filtering is applied, $\sigma_x^2 = \sigma_g^2 + 2\sigma_i^2$, where σ_i is the instrumental resolution, in this case 145 km s^{-1} . Note that the calibration curve flattens for $\sigma_g < \sigma_i$, indicating that the true dispersion becomes increasingly difficult to recover as it drops below the instrumental resolution.

were rejected. (ii) The mean ratio between the dispersions from a fiducial K0 template and each other template was used to scale all the dispersions from the other template to the dispersion scale of the fiducial. These dispersion scales differed by less than 5% for 90% of the templates. (iii) A mean dispersion for each galaxy was then computed from all the unrejected cases using 2-pass 2σ clipping. (iv) Any template with a scale differing by more than 10% from the mean was rejected as being a poor match to the programme galaxies and the entire procedure was then repeated. (Note that no significant correlation was found between scale factor and spectral type over the range G8 to K5 spanned by our templates.) The scatter in the dispersion estimates from different templates after this procedure was typically 3–4%.

Two corrections need to be applied to the velocity dispersions before they are fully calibrated: (i) an aperture correction to account for different effective apertures sampling different parts of the galaxy velocity dispersion profile, and (ii) a run correction to remove systematic scale errors between different observing setups. The latter type of correction is also applied to the redshifts to give them a common zeropoint. These two corrections are discussed below at §3.4 and §3.5 respectively.

3.2 Linestrength Indices

Once redshifts and velocity dispersions were determined, linestrength indices could also be measured using the prescription given by González (1993). This is a refinement of the original ‘Lick’ system in which a standard set of bands was defined for measuring linestrength indices for 11 features in the spectra of spheroidal systems (Burstein et al. 1984). González (1993), Worthey (1993) and Worthey et al. (1994) describe how this system has been updated and expanded to a set of 21 indices. Here we measure both the Mgb and Mg_2 indices.

The feature bandpass for Mgb index is $5160.1\text{--}5192.6\text{\AA}$, encompassing the Mg I triplet with components at 5166.6\AA , 5172.0\AA and 5183.2\AA . The continuum on either side of the absorption feature is defined in bands covering $5142.6\text{--}5161.4\text{\AA}$ and $5191.4\text{--}5206.4\text{\AA}$. Mgb is an *atomic* index, and so is defined as the equivalent width of the feature in Ångstroms,

$$\text{Mgb} = \int \left(1 - \frac{S(\lambda)}{C(\lambda)} \right) d\lambda, \quad (1)$$

where the integral is over the feature bandpass, $S(\lambda)$ is the object spectrum and $C(\lambda)$ is the linear pseudo-continuum defined by interpolating between two continuum estimates, taken at the midpoints of the blue and red continuum bands to be the mean values of the observed spectrum in those bands.

Closely related to Mgb is the Mg_2 index, for which the feature bandpass is $5154.1\text{--}5196.6\text{\AA}$ and the continuum bands are $4895.1\text{--}4957.6\text{\AA}$ and $5301.1\text{--}5366.1\text{\AA}$. This index measures both the Mg I atomic absorption and the broader MgH molecular absorption feature. Mg_2 is a *molecular* index, and so is defined as the mean ratio of flux to local continuum in magnitudes,

$$\text{Mg}_2 = -2.5 \log_{10} \left(\frac{\int S(\lambda)/C(\lambda) d\lambda}{\Delta\lambda} \right), \quad (2)$$

where the integral is over the Mg_2 feature bandpass, $\Delta\lambda=42.5\text{\AA}$ is the width of that bandpass, and the pseudo-continuum is interpolated from the Mg_2 continuum bands.

In fact we will often find it convenient to express the Mgb index in magnitudes rather than as an equivalent width. By analogy with the Mg_2 index, we therefore define Mgb' to be

$$\text{Mgb}' = -2.5 \log_{10} \left(1 - \frac{\text{Mgb}}{\Delta\lambda} \right), \quad (3)$$

where in this case $\Delta\lambda=32.5\text{\AA}$, the width of the Mgb feature bandpass.

In passing it should be noted that a different definition of linestrength indices has sometimes been used (e.g. Worthey 1994, equations 4 and 5) in which the integral of the ratio of the object spectrum and the continuum in equations 1 and 2 is replaced by the ratio of the integrals. This alternative definition has merits (such as simplifying the error properties of measured indices), but it is not mathematically equivalent to the standard definition. In practice, however, the two definitions generally give linestrengths with negligibly different numerical values.

It is usual in studies of this sort to employ the Mg_2 index as the main indicator of metallicity and star-formation

history. However we find it useful for operational reasons to also measure the *Mgb* index. One problem is that the limited wavelength coverage of the spectra from some runs means that in a number of cases we cannot measure the Mg_2 index (requiring as it does a wider wavelength range) although we can measure the *Mgb* index. We obtain *Mgb* for 676 objects (with 299 having repeat measurements) and Mg_2 for 582 objects (with 206 having repeat measurements). Another problem with Mg_2 is that the widely-separated continuum bands make it more susceptible than *Mgb* to variations in the non-linear continuum shape of our unfluxed spectra, which result from using a variety of different instruments and observing galaxies over a wide range in redshift. We therefore present measurements of both *Mgb* and Mg_2 : the former because it is better-determined and available for more sample galaxies, the latter for comparison with previous work. As previously demonstrated (Gorgas et al. 1990, Jørgensen 1997) and confirmed here, *Mgb* and Mg_2 are strongly correlated, and so can to some extent be used interchangeably.

Several corrections must be applied to obtain a linestrength measurement that is calibrated to the standard Lick system. The first correction allows for the fact that the measured linestrength depends on the instrumental resolution. Since all our spectra were obtained at higher resolution than the spectra on which the Lick system was defined, we simply convolve our spectra with a Gaussian of dispersion $(\sigma_{\text{Lick}}^2 - \sigma_i^2)^{1/2}$ in order to broaden our instrumental resolution σ_i (see Table 1) to the Lick resolution of 200 km s^{-1} .

The second correction allows for the fact that the measured linestrength depends on the galaxy’s internal velocity dispersion—a galaxy with high enough velocity dispersion σ_g will have features broadened to the point that they extend outside their index bandpasses, and so their linestrengths will be underestimated. Moreover, if an absorption feature is broadened into the neighbouring continuum bands then the estimated continuum will be depressed and the linestrength will be further reduced. The ‘ σ -correction’ needed to calibrate out this effect can be obtained either by measuring linestrength as a function of velocity broadening for a set of suitable stellar spectra (such as the templates obtained for measuring redshifts and dispersions) or by modelling the feature in question.

Although most previous studies have adopted the former approach, we prefer to use a model to calibrate our indices, since we observe a dependence of the *Mgb* profile shape on σ that is not taken into account by simply broadening stellar templates. Our simple model assumes *Mgb* to be composed of three Gaussians centred on the three Mg I lines at $\lambda_b=5166.6\text{\AA}$, $\lambda_c=5172.0\text{\AA}$ and $\lambda_r=5183.2\text{\AA}$ with corresponding relative strengths varying linearly with dispersion from 1.0:1.0:1.0 at $\sigma=100 \text{ km s}^{-1}$ to 0.2:1.0:0.7 at $\sigma=300 \text{ km s}^{-1}$. This dependence on dispersion is empirically determined and approximate (the relative strengths of the individual lines are not tightly constrained), but it does significantly improve the profile fits compared to assuming any fixed set of relative weights. Such variation of the *Mgb* profile shape reflects changes, as a function of velocity dispersion, in the stellar population mix and relative abundances (particularly of Mg, C, Fe and Cr), which each affect the profile in complex ways (Tripicco & Bell 1995).

Using the estimated value of the index to normalise the model profile and the effective dispersion $(\sigma_g^2 + \sigma_{\text{Lick}}^2)^{1/2}$

to give the broadening, we can estimate both the profile flux which is broadened out of the feature bandpass and the resulting depression of the continuum. Correcting for both these effects gives an improved estimate for the linestrength. Iterating leads rapidly to convergence and an accurate σ -correction for the *Mgb* and Mg_2 indices. We find that the *Mgb* σ -correction is typically +4% at 100 km s^{-1} and increases approximately linearly to +16% at 400 km s^{-1} ; the Mg_2 σ -correction is typically 0.000 mag up to 200 km s^{-1} and increases approximately linearly to 0.004 mag at 400 km s^{-1} .

Note that the usual method of determining the σ -correction by broadening standard stars ignores the dependence of profile shape on changes in the stellar population mix as a function of luminosity or velocity dispersion. Our tests indicate that by doing so, the usual method tends to overestimate *Mgb* for galaxies with large dispersions: by 2% at 200 km s^{-1} , 6% at 300 km s^{-1} and 14% at 400 km s^{-1} . The two methods give essentially identical results for Mg_2 , since it has much smaller σ -corrections due to its wider feature bandpass and well-separated continuum bands.

The other corrections that need to be applied to the linestrength estimates are: (i) an aperture correction to account for different effective apertures sampling different parts of the galaxy (§3.4); (ii) a run correction to remove systematic scale errors between different observing setups (§3.5); and (iii) an overall calibration to the Lick system determined by comparisons with literature data (§4.3).

3.3 Error Estimates

Error estimates for our redshifts, velocity dispersions and linestrengths come from detailed Monte Carlo simulations of the measurement process for each observing run. By calibrating the errors estimated from these simulations against the rms errors obtained from the repeat measurements that are available for many of the objects (see §3.6), we can obtain precise and reliable error estimates for each measurement of every object in our sample.

The procedure for estimating the uncertainties in our redshifts and velocity dispersions was as follows. For each stellar template in each observing run, we constructed a grid of simulated spectra with Gaussian broadenings of $100\text{--}300 \text{ km s}^{-1}$ in 20 km s^{-1} steps and continuum counts corresponding to S/N ratios of 10–90 in steps of 10. For each spectrum in this grid we generated 16 realisations assuming Poisson noise. These simulated spectra were then cross-correlated against all the other templates from the run in order to derive redshifts and velocity dispersions in the standard manner. The simulations do not account for spectral mismatch between the galaxy spectra and the stellar templates, but for well-chosen templates this effect is only significant at higher S/N than is typically found in our data.

Figure 4 shows the random error in redshift and the systematic and random errors in dispersion as functions of input dispersion and S/N for four of the larger runs. The systematic errors in redshift are not shown as they are negligibly small ($\sim 1 \text{ km s}^{-1}$), although the simulations do not include possible zeropoint errors. The systematic errors in dispersion are generally small (a few percent or less) for $S/N > 20$, but become rapidly larger at lower S/N . The random errors in redshift increase for lower S/N and higher dis-

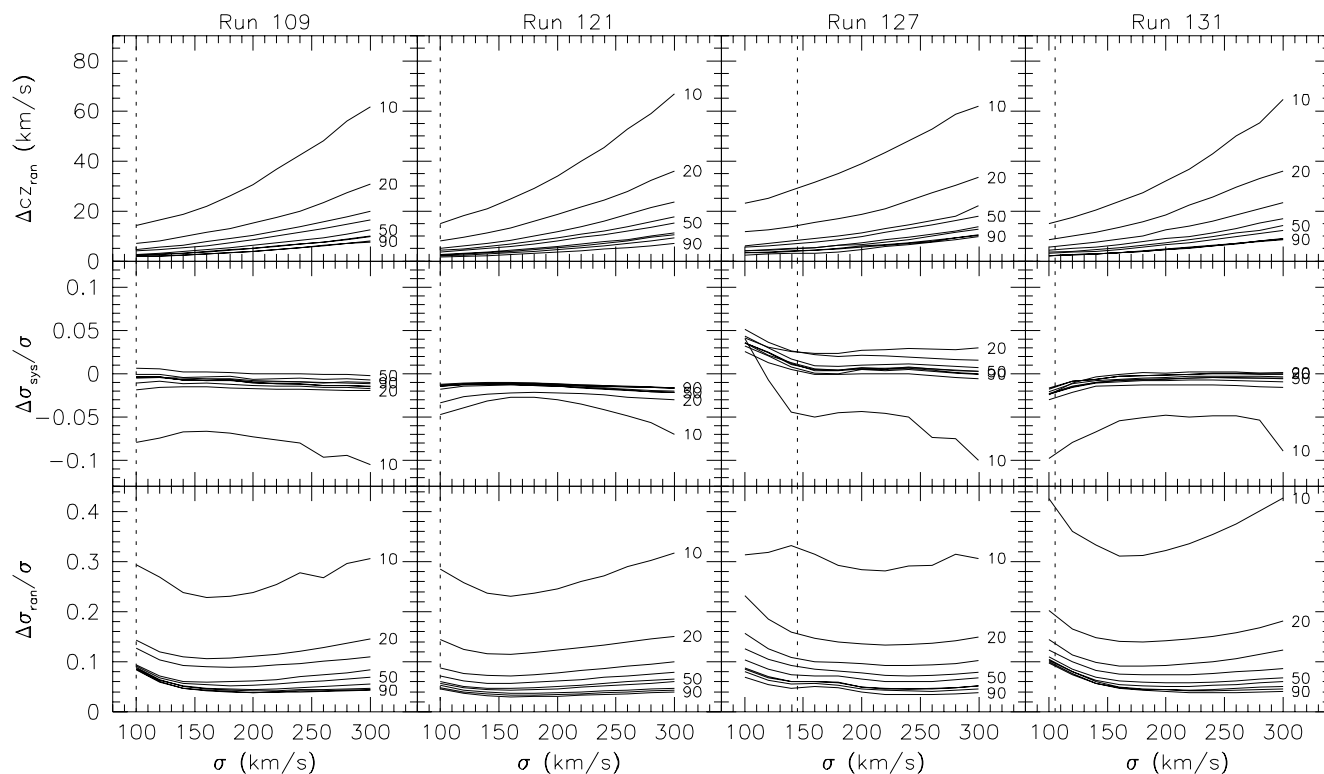


Figure 4. Redshift and dispersion errors as functions of input dispersion and S/N (labelling the curves) from the simulations of four of the larger runs. The top panel shows the random error in the redshift and the centre and bottom panels show the systematic and random error in the dispersion. The vertical dotted line indicates the instrumental dispersion of each run.

persion, while the random errors in dispersion increase for lower S/N but have a broad minimum at around twice the instrumental dispersion. These curves have the general form predicted for the random errors from the cross-correlation method (Tonry & Davis 1979, Colless 1987).

Given the dispersion and S/N measured for a spectrum, we interpolated the error estimates from the simulation for that particular observing run to obtain the systematic and random errors in each measured quantity. We used the results of these simulations to correct the systematic errors in the velocity dispersions and to estimate the uncertainties in individual measurements of redshift and dispersion. For quality class D measurements of redshifts, where the spectra are too poor to estimate a dispersion and hence a reliable redshift error, we take a conservative redshift error of 50 km s^{-1} .

The linestrength error estimates were obtained by generating 50 Monte Carlo realizations of the object spectrum with Poisson noise appropriate to the spectrum’s S/N level. The Mgb and Mg_2 linestrengths were then measured for each of these realizations and the error estimated as the rms error of these measurements about the observed value. The error estimate obtained in this fashion thus takes into account the noise level of the spectrum, but does not account for errors in the linestrength due to errors in the redshift and dispersion estimates, nor for systematic run-to-run differences in the underlying continuum shape.

The estimated errors in the spectroscopic parameters

are compared with, and calibrated to, the rms errors derived from repeat observations in §3.6.

3.4 Aperture Corrections

The velocity dispersion measured for a galaxy is the luminosity-weighted velocity dispersion integrated over the region of the galaxy covered by the spectrograph aperture. It therefore depends on (i) the velocity dispersion profile; (ii) the luminosity profile; (iii) the distance of the galaxy; (iv) the size and shape of the spectrograph aperture; and (v) the seeing in which the observations were made. In order to intercompare dispersion measurements it is therefore necessary to convert them to a standard scale. The ‘aperture correction’ this requires has often been neglected because it depends in a complex manner on a variety of quantities some of which are poorly known. The neglect of such corrections may account in part for the difficulties often found in reconciling dispersion measurements from different sources.

The aperture correction applied by Davies et al. (1987) was derived by measuring dispersions for a set of nearby galaxies through apertures of $4'' \times 4''$ and $16'' \times 16''$. In this way they used their nearby galaxies to define the velocity dispersion profile and obtained a relation between the corrected value, σ_{cor} , and the observed one, σ_{obs} . This turned out to be an approximately linear relation amounting to a 5% correction over the distance range between Virgo and Coma.

More recently Jørgensen et al. (1995) have derived an

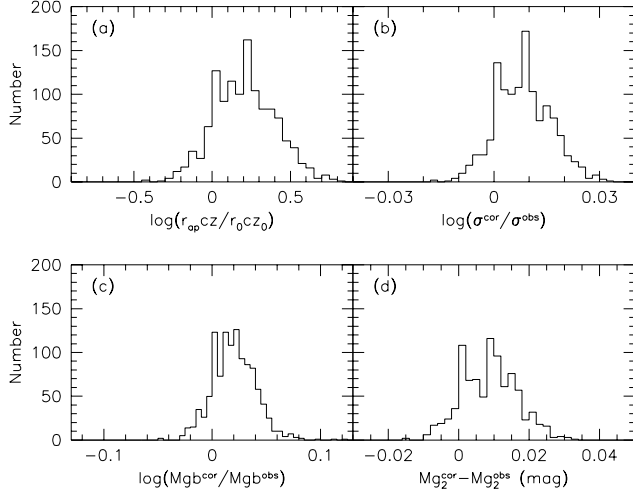


Figure 5. The distribution of aperture corrections to a standard metric aperture. (a) The distribution of the ratio of the observed metric apertures to the standard metric aperture (corresponding to 1.7 arcsec at the redshift of Coma). (b)-(d) The aperture corrections to this standard metric aperture for the dispersion, Mgb and Mg_2 measurements. Note that σ^{cor} is the aperture-corrected dispersion and σ^{obs} is the raw observed dispersion; likewise for the linestrengths.

aperture correction from kinematic models based on data in the literature. Published photometry and kinematics for 51 galaxies were used to construct two-dimensional models of the surface brightness, velocity dispersion, and rotational velocity projected on the sky. They found that the position angle only gave rise to 0.5% variations in the derived dispersions and could thus be ignored. They converted rectangular apertures into an ‘equivalent circular aperture’ of radius r_{ap} which the models predicted would give the same dispersion as the rectangular slit. They found that to an accuracy of 4% one could take $r_{ap} = 1.025(xy/\pi)^{1/2}$, where x and y are the width and length of the slit.

From their models they then calculated the correction factor from the observed dispersion to the dispersion in some standard aperture. For a standard *metric* aperture, they found this aperture correction to be well approximated by a power law of the form

$$\frac{\sigma_{cor}}{\sigma_{obs}} = \left[\left(\frac{r_{ap}}{r_0} \right) \left(\frac{cz}{cz_0} \right) \right]^{0.04}, \quad (4)$$

where σ_{obs} and σ_{cor} are the observed and corrected dispersions, r_0 is a standard aperture radius, defined to be 1.7 arcsec, and cz_0 is a standard redshift, defined as the redshift of Coma. The standard metric aperture is thus $0.54 \text{ h}^{-1} \text{ kpc}$ in radius. Alternatively, one can correct to a standard *relative* aperture (defined to be $R_e/8$) using the same power law relation,

$$\frac{\sigma_{cor}}{\sigma_{obs}} = \left(\frac{r_{ap}}{R_e/8} \right)^{0.04}. \quad (5)$$

This power law approximates the true relation to within 1% over the observed range of effective apertures (compare the distribution metric aperture sizes in Figure 5a with Figure 4c of Jørgensen et al.).

We also apply an aperture correction to our

linestrengths. Jørgensen et al. noted that the radial gradient in the Mg_2 index is similar to the radial gradient in $\log \sigma$, and so applied the same aperture correction for Mg_2 as for $\log \sigma$. We adopt this procedure for Mg_2 . For Mgb we convert to Mgb' (Equation 3) and, assuming that the radial profile of Mgb' is similar to that of Mg_2 (and hence $\log \sigma$), we apply the $\log \sigma$ aperture correction to Mgb' before converting back to Mgb .

The distributions of corrections to the standard metric aperture for the dispersions and linestrengths are shown in Figures 5b-d. These corrections are generally positive, as most objects in our sample are observed through larger effective apertures and are further away than Jørgensen et al.’s standard aperture and redshift. The corrections to standard relative apertures are quite similar, although having slightly greater amplitude and range. We choose to adopt the correction to a standard metric aperture in order to minimise the size and range of the corrections and to facilitate comparisons with dispersions and linestrengths in the literature.

3.5 Combining Different Runs

In comparing the redshifts, dispersions and linestrengths obtained from different runs we found some significant systematic offsets. The origin of these run-to-run offsets is not fully understood. For the redshifts, the use of different velocity standard stars as the fiducials in different runs clearly contributes some systematic errors. For the dispersions, the calibration procedure we use should in principle remove instrumental systematics; in practice, scale differences are common, as is shown by the range of scale factors needed to reconcile velocity dispersions from various sources in the compilation by McElroy (1995; see Table 2).

We cannot directly calibrate the measurements from each run to the system defined by a chosen fiducial run, as there is no run with objects in common with all other runs to serve as the fiducial. Instead, we use the mean offset, Δ , between the measurements from any particular run and *all* the other runs. To compute this offset we separately compute, for each galaxy i , the error-weighted mean value of the measurements obtained from the run in question, x_{ij} , and from all other runs, y_{ik} :

$$\langle x_i \rangle = \frac{\sum_j x_{ij}/\delta_{ij}^2}{\sum_j 1/\delta_{ij}^2}, \quad \langle y_i \rangle = \frac{\sum_k y_{ik}/\delta_{ik}^2}{\sum_k 1/\delta_{ik}^2}. \quad (6)$$

Here j runs over the m_i observations of galaxy i in the target run and k runs over the n_i observations of galaxy i in all other runs; δ_{ij} and δ_{ik} are the estimated errors in x_{ij} and y_{ik} . We then take the average over all galaxies, weighting by the number of comparison pairs, to arrive at an estimate for the offset of the target run:

$$\Delta = \frac{\sum_i m_i n_i (\langle x_i \rangle - \langle y_i \rangle)}{\sum_i m_i n_i} \quad (7)$$

Here i runs over the l galaxies in the sample. We can reject outliers at this point by excluding galaxies for which the difference $\langle x_i \rangle - \langle y_i \rangle$ is larger than some cutoff: for cz , $\log \sigma$, Mgb' and Mg_2 we required differences less than 300 km s^{-1} , 0.2 dex, 0.1 mag and 0.1 mag respectively. The uncertainty, ϵ , in this estimate of the run offset is given by

Table 2. Calibration of observing runs to a common system.

Run	Δcz (km s^{-1})	N_z	N_z^c	$\Delta \log \sigma$ (dex)	N_σ	N_σ^c	$\Delta \text{Mgb}'$ (mag)	N_b	N_b^c	ΔMg_2 (mag)	N_2	N_2^c
101	-9 ± 9	19	62	$+0.014 \pm 0.016$	18	65	$+0.009 \pm 0.009$	18	32	-0.008 ± 0.007	16	30
102	$+62 \pm 10$	56	57	$+0.034 \pm 0.023$	56	56	$+0.012 \pm 0.011$	56	24	-0.013 ± 0.010	56	12
103	-43 ± 10	36	53	-0.034 ± 0.028	34	48	-0.002 ± 0.011	34	27	-0.025 ± 0.009	34	20
104 ^b	+0	11	0	+0.000	11	0	+0.000	11	0	+0.000	11	0
105	$+16 \pm 9$	36	54	$+0.018 \pm 0.019$	36	55	$+0.020 \pm 0.007$	36	37	$+0.008 \pm 0.009$	21	14
106	-17 ± 14	23	61	$+0.024 \pm 0.029$	22	54	$+0.009 \pm 0.007$	22	41	$+0.001 \pm 0.014$	14	13
107	-19 ± 10	27	61	$+0.060 \pm 0.033$	27	64	$+0.000 \pm 0.009$	27	33	-0.003 ± 0.008	21	24
108	-71 ± 23	9	35	-0.055 ± 0.035	9	34	-0.005 ± 0.008	9	12	$+0.032 \pm 0.008$	9	11
109 ^a	$+1 \pm 4$	93	222	-0.015 ± 0.005	92	220	$+0.000 \pm 0.000$	92	167	$+0.008 \pm 0.002$	92	126
110	$+3 \pm 6$	71	186	-0.010 ± 0.008	61	171	$+0.004 \pm 0.004$	61	78	-0.009 ± 0.004	61	50
111	-10 ± 14	19	72	-0.024 ± 0.024	19	76	-0.005 ± 0.006	19	33	$+0.046 \pm 0.006$	19	25
112	$+45 \pm 8$	31	82	-0.006 ± 0.008	31	103	$+0.001 \pm 0.009$	31	16	-0.027 ± 0.013	16	7
113	$+154 \pm 15$	20	9	$+0.041 \pm 0.038$	20	9	$+0.025 \pm 0.012$	20	7	-0.015 ± 0.026	2	1
114	-9 ± 11	12	22	-0.059 ± 0.024	12	22	-0.012 ± 0.009	12	20	$+0.032 \pm 0.007$	12	15
115	$+9 \pm 10$	8	24	$+0.024 \pm 0.022$	8	23	-0.069 ± 0.026	1	2	-0.087 ± 0.034	1	2
116 ^d	—	—	—	—	—	—	—	—	—	—	—	—
117	-2 ± 7	59	132	$+0.005 \pm 0.021$	55	121	$+0.016 \pm 0.007$	55	90	$+0.028 \pm 0.007$	41	51
118 ^c	$+120 \pm 22$	14	4	-0.018 ± 0.066	13	4	-0.011 ± 0.029	13	3	+0.000	5	0
119	-20 ± 9	17	20	-0.004 ± 0.015	17	19	$+0.003 \pm 0.007$	17	19	-0.013 ± 0.009	17	8
120	-39 ± 7	38	47	$+0.009 \pm 0.011$	34	44	$+0.005 \pm 0.005$	33	25	$+0.059 \pm 0.008$	26	14
121	-66 ± 8	86	177	$+0.038 \pm 0.010$	82	181	$+0.002 \pm 0.008$	82	23	$+0.008 \pm 0.008$	54	17
122	-28 ± 8	41	70	$+0.001 \pm 0.012$	37	58	$+0.020 \pm 0.006$	37	32	$+0.033 \pm 0.008$	31	24
123	-22 ± 8	22	41	$+0.022 \pm 0.017$	17	34	$+0.005 \pm 0.006$	16	26	$+0.010 \pm 0.006$	13	16
124	$+14 \pm 17$	22	49	$+0.020 \pm 0.044$	14	40	$+0.029 \pm 0.012$	14	8	$+0.012 \pm 0.022$	11	1
125	-48 ± 14	57	62	$+0.037 \pm 0.010$	55	64	$+0.007 \pm 0.008$	55	8	-0.018 ± 0.011	55	7
126	$+57 \pm 14$	36	43	-0.004 ± 0.039	33	40	$+0.029 \pm 0.023$	33	9	$+0.008 \pm 0.023$	33	6
127	-3 ± 4	131	187	$+0.002 \pm 0.007$	127	167	-0.007 ± 0.003	127	136	-0.007 ± 0.003	127	83
128	$+6 \pm 12$	24	29	-0.042 ± 0.010	23	29	$+0.010 \pm 0.015$	23	7	-0.055 ± 0.013	9	4
129 ^b	+0	3	0	+0.000	3	0	+0.000	3	0	+0.000	3	0
130 ^d	—	—	—	—	—	—	—	—	—	—	—	—
131 ^e	$+35 \pm 5$	123	174	-0.078 ± 0.014	99	152	$+0.002 \pm 0.004$	98	136	—	—	—
132	-24 ± 19	12	7	-0.025 ± 0.026	12	6	-0.032 ± 0.008	12	4	$+0.005 \pm 0.016$	12	4
133	-11 ± 4	128	247	-0.009 ± 0.006	128	241	-0.009 ± 0.002	128	183	-0.014 ± 0.002	128	151

^a Run 109 is the fiducial run for Mgb' , defined to have zero offset.

^b Runs 104 and 129 have no objects in common with other runs.

^c Run 118 has no Mg_2 measurements in common with other runs.

^d Runs 116 and 130 have no usable data.

^e Run 131 has no Mg_2 measurements.

$$\epsilon^2 = \frac{\sum_i (m_i n_i)^2 (\delta \langle x_i \rangle^2 + \delta \langle y_i \rangle^2)}{(\sum_i m_i n_i)^2} \quad (8)$$

where $\delta \langle x_i \rangle$ and $\delta \langle y_i \rangle$ are the error-weighted uncertainties in $\langle x_i \rangle$ and $\langle y_i \rangle$ given by

$$\delta \langle x_i \rangle^2 = \left(\sum_j \delta_{ij}^{-2} \right)^{-1}, \quad \delta \langle y_i \rangle^2 = \left(\sum_k \delta_{ik}^{-2} \right)^{-1}. \quad (9)$$

We subtract the offset determined in this manner from each run and then iterate the whole procedure until there are no runs with residual offsets larger than 0.5ϵ . As a final step, we place the entire dataset (now corrected to a common zeropoint) onto a fiducial system by subtracting from all runs the offset of the fiducial system. Note that the run corrections for dispersion and Mgb are determined in terms of offsets in $\log \sigma$ and Mgb' .

In order to maximise the number of objects with multiple measurements, we included the dataset from the ‘Streaming Motions of Abell Clusters’ project (SMAC: M.J.Hudson, priv.comm.; see also Smith et al. 1997) in this analysis. There is a considerable overlap between the SMAC and EFAR samples which significantly increases the number

of comparison observations and reduces the uncertainties in the run offsets. We chose to use the ‘Lick’ system of Davies et al. (1987; included in the SMAC dataset) as our fiducial, in order to bring the 7 Samurai, EFAR and SMAC datasets onto a single common system. This is not possible with Mgb , which is not measured in most previous work or by SMAC. We therefore chose run 109 (the Kitt Peak 4m run of November 1988) as the Mgb fiducial because it had a large number of high-quality observations and the systematics of the slit spectrograph are believed to be well understood.

We checked that this procedure gives relative run corrections consistent with those obtained by directly comparing runs in those cases where there *are* sufficient objects in common. We have also compared our method with a slightly different method used by the SMAC collaboration to determine the run corrections for their own data and found good agreement (M.J.Hudson, priv.comm.). We carried out Monte Carlo simulations of the whole procedure in order to check the uncertainties in the offsets computed according to Equation 8. We found that this equation in general provides a good estimate of the uncertainties, although when

the number of comparisons is small or involve a small number of other runs it can under-estimate the uncertainties by up to 30%. Our final estimates of the uncertainties are therefore derived as the rms of the offsets from 100 Monte Carlo simulations.

Table 2 lists the offsets for each run computed according to the above procedure, their uncertainties based on Monte Carlo simulations, the number of individual measurements (N) and the number of comparison pairs (N^c). Note that to correct our observed measurements to the fiducial system we *subtract* the appropriate run offset in Table 2 from each individual measurement. Of the 31 spectroscopic runs with usable data, only runs 104 and 129 have no objects in common with other runs and hence no run corrections; run 118 has no Mg_2 measurements in common and so no run correction for Mg_2 .

Weighting by the number of individual measurements in each run, the mean amplitude of the corrections and their uncertainties are $28 \pm 8 \text{ km s}^{-1}$ in cz , 0.023 ± 0.015 dex in $\log \sigma$, 0.008 ± 0.006 mag in Mgb' and 0.015 ± 0.006 mag in Mg_2 . The significance of the individual run corrections (in terms of the ratio of the amplitude of the offset to its uncertainty) varies; however over all runs the reduced χ^2 is highly significant: 15.7, 4.0, 3.3 and 11.4 for the corrections to the redshifts, dispersions, Mgb and Mg_2 respectively. Application of the run corrections reduces the median rms error amongst those objects with repeat measurements from 18 km s^{-1} to 14 km s^{-1} in redshift, 6.3% to 5.6% in dispersion, 4.9% to 4.4% in Mgb and 0.012 mag to 0.009 mag in Mg_2 . We also checked to see whether applying the run corrections reduced the scatter in external comparisons between our data and measurements in the literature (see 4.3). We found that although the scatter is dominated by the combined random errors, the corrections did reduce the scatter slightly in all cases.

As another test of the run corrections for Mgb' and Mg_2 (and also, more weakly, for $\log \sigma$), we compared the $Mgb'-\sigma$ and $Mg_2-\sigma$ distributions for each run (after applying the run corrections) with the global $Mgb'-\sigma$ and $Mg_2-\sigma$ relations derived in Paper V. Using the χ^2 goodness-of-fit statistic to account both for measurement errors in the dispersions and linestrengths and for the intrinsic scatter about the $Mg-\sigma$ relations, we find that for $Mgb'-\sigma$ there were two runs (113 and 132) with reduced χ^2 greater than 3, while for $Mg_2-\sigma$ there was one such run (122). In all three cases the removal of 1 or 2 obvious outliers decreased the reduced χ^2 to a non-significant level.

3.6 Calibrating the Estimated Errors

Obtaining precise error estimates is particularly important because we will make extensive use of them in applying maximum likelihood methods to deriving the Fundamental Plane and relative cluster distances for our sample. Although we have estimated the measurement errors as carefully as possible, simulating the noise in the observations and the measurement procedures, some sources of error are likely to remain unaccounted-for and we may be systematically mis-estimating the errors. We therefore auto-calibrate our errors by scaling the estimated errors in the combined measurements (the *internal* error estimate, based on the individual measurement errors derived from simulations; see

§3.3 and §4.2) to match the rms errors from objects with repeat measurements (an *external* error estimate).

Figure 6 shows the differential and cumulative distributions of the ratio of the rms error to the estimated error for each galaxy with repeat measurements of redshift, dispersion, Mgb and Mg_2 . The smooth curves are the predicted differential and cumulative distributions of this ratio assuming that the estimated errors are the true errors. The top panel shows the comparison using the estimated errors (including all the corrections discussed above). For the redshifts and linestrengths, the estimated errors are generally under-estimates of the true errors, since the ratio of rms to estimated errors tends to be larger than predicted. For the dispersions the estimated errors are generally over-estimates of the true errors, since this ratio tends to be smaller than predicted. For all quantities the assumption that the estimated errors are consistent with the true errors is ruled out with high confidence by a Kolmogorov-Smirnov (KS) test applied to the observed and predicted cumulative distributions. These differences between the estimated errors from the simulations and the rms errors from repeat measurements reflect the approximate nature of the S/N estimates and systematic measurement errors not accounted for in the simulations.

In order to bring our estimated errors into line with the rms errors from the repeat measurements, we found it necessary to add 15 km s^{-1} in quadrature to the estimated redshift errors, to scale the dispersion and Mgb errors by factors of 0.85 and 1.15 respectively, and to add 0.005 mag to the Mg_2 errors. These corrections were determined by maximising the agreement of the observed and predicted distributions of the ratio of rms to estimated errors under a KS test (excluding outliers with values of this ratio > 3.5). The corrections are quite well determined: to within a couple of km s^{-1} for the redshift correction, a few percent for the dispersion and Mgb corrections, and 0.001 mag for the Mg_2 correction. Applying these corrections and repeating the comparison of rms and estimated errors gives the lower panels of Figure 6, which shows the good agreement between the rms errors from repeat measurements and the calibrated errors estimates for the redshifts, dispersions and Mg linestrengths.

The need for such a correction to the redshift errors may be due in part to the residual zeropoint uncertainties in the redshifts and in part to a tendency for the simulations to under-estimate the errors for high S/N spectra. The origin of the over-estimation of the dispersion errors is uncertain, although it may result from slightly different prescriptions for estimating the S/N in the observations and the simulations. The under-estimation of the linestrength errors may be due to neglecting the effects of errors in the redshift and dispersion estimates and the different continuum shapes of spectra from different runs when measuring linestrengths.

4 RESULTS

4.1 Individual Measurements

The previous two sections describe the observations and analysis of our spectroscopic data. Table 3 lists the observational details for each spectrum and the fully-corrected measurements of redshift, dispersion, Mgb and Mg_2 , together

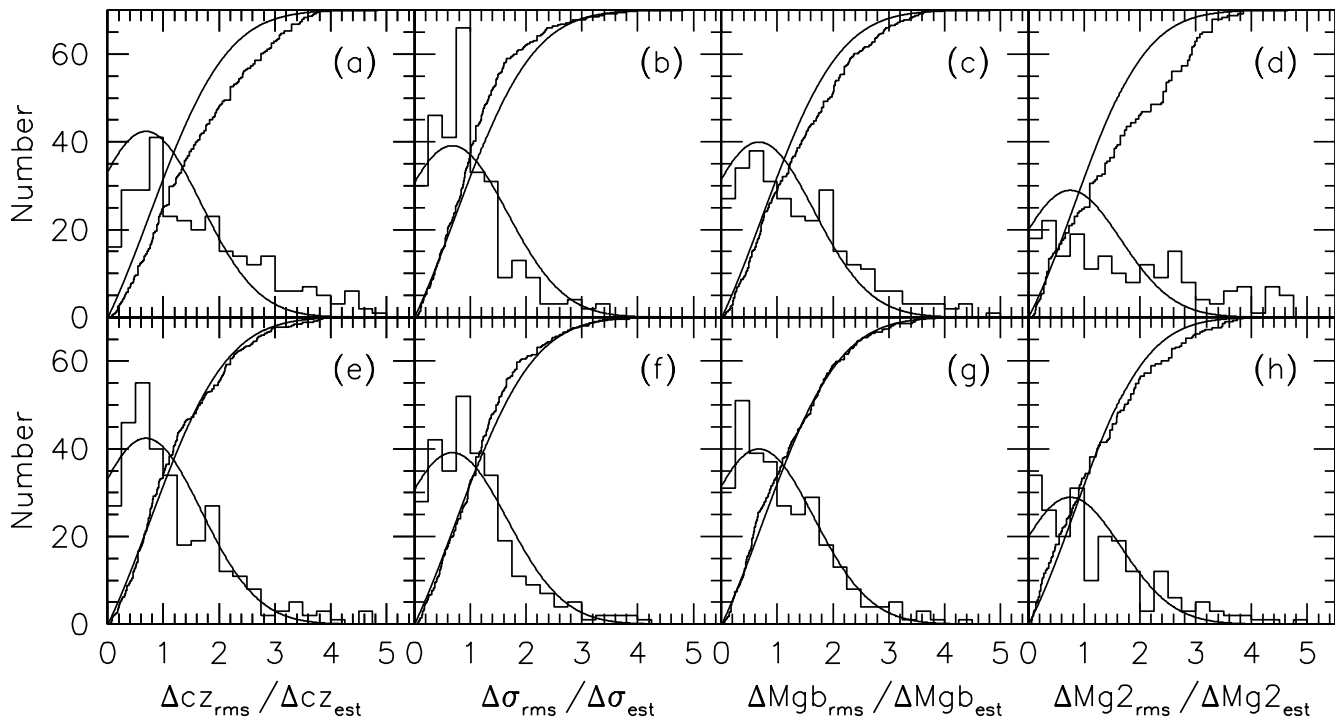


Figure 6. Comparison of the estimated errors derived from simulations and the rms errors for galaxies with repeat measurements of redshift, dispersion, Mgb and Mg₂. Each panel shows the differential and cumulative distributions of the ratio of rms error to estimated error. The stepped curves are the observed distributions, while the smooth curves are the predicted distributions. The upper panels show the comparisons using the original estimated errors; the lower panels show the comparisons after correcting the estimated errors as described in the text.

with their calibrated error estimates. Note that these error estimates are the individual measurement errors, and must be combined in quadrature with the run correction uncertainties given in Table 2 to give the total error estimate. We list the measurement errors rather than the total errors because the total errors are not independent, being correlated for objects in the same run. The version of the table presented here is abridged; the full table will be available upon publication from NASA’s Astrophysical Data Center (ADC) and from the Centre de Données astronomiques de Strasbourg (CDS).

The entries in Table 3 are as follows: Column 1 gives GINRUNSEQ, a unique nine-digit identifier for each spectrum, composed of the galaxy identification number (GIN) as given in the master list of EFAR sample galaxies (Table 3 of Paper I), the run number (RUN) as given in Table 1, and a sequence number (SEQ) which uniquely specifies the observation within the run; column 2 gives the galaxy name, as in the master list of Paper I; column 3 is the telescope code, as in Table 1; column 4 is the UT date of the observation; columns 5 & 6 are the quality parameter (with an asterisk if the spectrum shows emission features) and S/N of the spectrum (see §2.4); columns 7 & 8 are the fully-corrected heliocentric redshift cz (in km s^{-1}) and its measurement error; columns 9 & 10 are the fully-corrected velocity dispersion σ (in km s^{-1}) and its measurement error; columns 11 & 12 are the fully-corrected Mgb linestrength index and its measurement error (in \AA); columns 13 & 14 are the fully-corrected Mg₂ linestrength index and its measurement error (in mag);

column 15 provides comments, the full meanings of which are described in the notes to the table.

There are 1319 spectra in this table. Note that 81 objects from our original sample do not have spectroscopic observations and do not appear in the table (see the list of missing GINs in the table notes). Three of these are the duplicate objects (GINs 55, 435, 476) and three are known stars (GINs 131, 133, 191). Most of the others are objects which our imaging showed are not early-type galaxies, although there are a few early-type galaxies for which we did not get a spectrum. There are 34 spectra which are unusable ($Q=E$) either because the spectrum is too poor (13 cases) or because the object was mis-identified (20 cases) or is a known star (1 case, GIN 123). Of the 1285 usable spectra (for 706 different galaxies), there are 637 spectra with $Q=A$, 407 with $Q=B$, 161 with $Q=C$ and 80 with $Q=D$.

The cumulative distributions of the total estimated errors in the individual measurements (combining measurement errors and run correction uncertainties in quadrature) are shown in Figure 7 for quality classes A, B and C, and for all three classes together. The error distributions can be quantitatively characterised by their 50% and 90% points, which are listed in Table 4. The overall median error in a single redshift measurement is 22 km s^{-1} , the median relative errors in single measurements of dispersion and Mgb are 10.5% and 8.2%, and the median error in a single measurement of Mg₂ is 0.015 mag.

Table 3. Individual spectroscopic measurements (abridged)

(1)	(2)	(3)	(4)	(5)	(6)	(7)	(8)	(9)	(10)	(11)	(12)	(13)	(14)	(15)
GINRUNSEQ	Galaxy Name	Telescope	Obsv Date	Q	S/N	cz (km s^{-1})	σ (km s^{-1})	Mgb (\AA)	Mg_2 (mag)					Notes
001106215	A76 A	MG24	880914	A	21.4	11296	51	262	50	5.20	0.54	0.353	0.020	
002106221	A76 B	MG24	880914	B	18.8	11317	47	225	47	4.76	0.59	0.326	0.019	
003106218	A76 C	MG24	880914	A	17.8	11973	49	217	48	5.17	0.68	0.392	0.021	
004107095	A76 D	MG24	881011	C	14.8	12184	31	316	103	6.18	0.83	0.326	0.028	
005120504	A76 E	IN25	901016	B	33.2	12241	19	217	16	6.35	0.22	0.312	0.011	
005120505	A76 E	IN25	901017	B	32.8	12147	17	169	11	6.16	0.23	0.275	0.012	
006107098	A76 F	MG24	881011	B	17.6	12371	28	307	82	5.29	0.83	0.331	0.027	
008122534	A85 A	MG24	911016	B	18.7	16577	39	290	52	5.14	0.59	0.344	0.021	
008123319	A85 A	IN25	911201	D	21.4	16692	50	—	—	—	—	—	—	
009120626	A85 B	IN25	901017	A	37.6	17349	34	436	46	5.74	0.22	—	—	
010120628	A85 C	IN25	901017	D	33.9	22837	50	—	—	—	—	—	—	Mgb at sky
011122540	A85 1	MG24	911016	B	25.8	15112	20	195	18	3.82	0.39	0.253	0.016	
012132001	A85 2	SS2B	931022	B	28.3	16264	25	294	32	5.86	0.31	0.337	0.011	
013101059	A119 A	MG24	861202	B	16.5	11516	49	299	48	6.06	0.51	0.294	0.022	
013109339	A119 A	KP4M	881107	A	44.2	11457	19	289	18	5.00	0.20	0.320	0.010	
013131330	A119 A	ES36	931008	A	30.9	11451	24	320	29	4.86	0.26	—	—	
014101063	A119 B	MG24	861202	C	14.4	13205	63	323	65	5.90	0.72	0.320	0.025	
014109339	A119 B	KP4M	881107	A	35.0	13345	21	276	21	4.86	0.22	0.361	0.010	
015109343	A119 C	KP4M	881107	A	33.2	13508	19	250	19	5.51	0.22	0.295	0.011	
015131330	A119 C	ES36	931008	B	19.5	13484	28	265	35	5.88	0.48	—	—	
016109346	A119 D	KP4M	881107	C*	20.8	14980	16	104	13	3.30	0.37	0.151	0.016	H β
016110611	A119 D	KP2M	881114	D*	15.6	15022	50	—	—	—	—	—	—	H β
016131330	A119 D	ES36	931008	D*	16.1	14996	50	—	—	—	—	—	—	H β
017109347	A119 E	KP4M	881107	A	36.1	12807	19	251	17	5.18	0.18	0.326	0.010	
017131330	A119 E	ES36	931008	A	27.0	12788	21	243	22	6.01	0.32	—	—	
018109342	A119 F	KP4M	881107	B	28.4	13034	18	193	15	4.95	0.32	0.245	0.013	
018131330	A119 F	ES36	931008	C	21.1	13006	16	112	20	4.69	0.37	—	—	
019109342	A119 G	KP4M	881107	E	32.7	—	—	—	—	—	—	—	—	mis-ID
019131330	A119 G	ES36	931008	A	36.7	13457	19	267	19	4.78	0.20	—	—	
021122654	A119 I	MG24	911018	A	31.0	13271	20	225	19	4.85	0.38	0.326	0.014	
022131330	A119 J	ES36	931008	B	22.3	13520	21	219	24	4.55	0.33	—	—	
023131330	A119 1	ES36	931008	C*	11.5	4127	18	92	38	0.50	0.78	—	—	H β
024122657	A119 2	MG24	911018	E	28.9	—	—	—	—	—	—	—	—	mis-ID
024131330	A119 2	ES36	931008	B	20.4	12346	16	100	20	5.13	0.38	—	—	
025107103	J3 A	MG24	881011	B	15.2	14453	32	333	111	6.25	0.74	0.329	0.025	
026120714	J3 B	IN25	901018	A	39.5	13520	18	231	15	4.93	0.23	—	—	
027107106	J3 C	MG24	881011	C	15.8	13771	21	163	38	4.33	0.86	0.224	0.027	
028120712	J3 D	IN25	901017	A	36.3	14316	22	287	23	5.45	0.24	—	—	double
028120713	J3 D	IN25	901017	B	30.8	14837	19	207	15	4.87	0.26	—	—	double
031107190	J4 A	MG24	881012	C	13.2	12074	24	185	51	5.35	0.75	0.387	0.029	
032107189	J4 B	MG24	881012	C	13.3	12090	31	302	102	4.11	1.08	0.261	0.032	
033132002	J4 C	SS2B	931021	A	30.0	17154	30	358	43	6.20	0.26	0.355	0.010	
036107195	A147 A	MG24	881012	C	12.2	12811	26	208	62	3.96	1.16	0.288	0.034	
036117298	A147 A	MG24	891015	B	19.0	12741	35	281	49	4.84	0.60	0.314	0.022	
036133157	A147 A	CT4M	931019	A	61.4	12760	17	235	12	4.77	0.17	0.285	0.010	
036133158	A147 A	CT4M	931019	A	62.3	12776	17	253	13	5.01	0.18	0.289	0.010	

This is an abridged version of this table; the full table will be available upon publication from NASA’s Astrophysical Data Center (ADC) and from the Centre de Donn es astronomiques de Strasbourg (CDS). The columns of this table give: (1) observation identifier (GINRUNSEQ); (2) galaxy name; (3) telescope used; (4) date of observation; (5) quality parameter; (6) signal to noise ratio; (7–8) redshift and estimated error; (9–10) velocity dispersion and estimated error; (11–12) Mgb linestrength and estimated error; (13–14) Mg₂ linestrength and estimated error; and (15) notes on each observation. In the notes, ‘double’ means the EFAR galaxy is double; ‘star’ means the EFAR object is a star not a galaxy; ‘mis-ID’ means the spectrum is for some galaxy other than the nominated EFAR object; ‘mis-ID*’ means the spectrum is for a nearby star rather than the EFAR object; ‘Mgb at sky’ means the object is at a redshift which puts Mgb on the 5577Å sky line; ‘#=#’ notes the duplicated pairs in the EFAR sample (see Paper I; only the first of the two GINs is used); emission line objects (with an asterisk on Q) have the emission features listed; ‘H β abs’ or ‘H β abs, [OIII]’ means the redshift is based on the H β absorption feature (and [OIII] if present), as the spectrum stops short of Mgb (no dispersion or Mgb index is given for these objects). The objects for which we have no spectrum have GINs: 7, 20, 29, 30, 34, 35, 55, 62, 64, 67, 82, 83, 91, 104, 121, 131, 133, 134, 161, 181, 191, 214, 225, 228, 231, 234, 256, 265, 309, 327, 391, 405, 407, 417, 434, 435, 442, 450, 451, 452, 458, 463, 464, 465, 470, 475, 477, 483, 484, 486, 494, 516, 520, 521, 522, 523, 526, 544, 551, 553, 567, 569, 570, 575, 576, 577, 587, 594, 597, 603, 605, 624, 625, 644, 671, 727, 760, 793, 798, 801, 901.

Table 4. The distribution of estimated errors per measurement

Q	Δcz (km/s)		$\Delta\sigma/\sigma$		$\Delta Mgb/Mgb$		ΔMg_2 (mag)	
	50%	90%	50%	90%	50%	90%	50%	90%
All	22	40	0.105	0.255	0.082	0.184	0.015	0.028
A	20	33	0.076	0.163	0.061	0.125	0.013	0.022
B	24	43	0.140	0.275	0.104	0.192	0.018	0.028
C	25	48	0.181	0.343	0.136	0.303	0.024	0.036

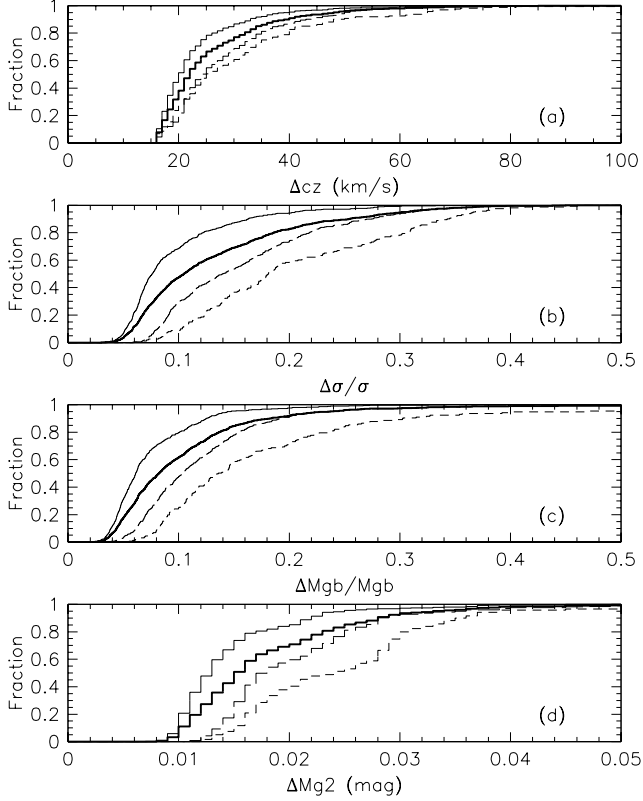


Figure 7. The cumulative distributions of estimated errors for individual measurements of redshift, velocity dispersion and Mgb linestrength. The distributions for quality classes A, B and C are shown as full, long-dashed and short-dashed lines respectively; the overall distribution is the thick full line. (a) The distribution of estimated errors in cz ; (b) estimated relative errors in σ ; (c) estimated relative errors in Mgb; (d) estimated errors in Mg_2 .

4.2 Combining Measurements

We use a weighting scheme to combine the individual measurements of each quantity to obtain a best estimate (and its uncertainty) for each galaxy in our sample. The weighting has three components:

(i) *Error weighting:* For multiple measurements X_i having estimated total errors Δ_i (the measurement errors and run correction uncertainties added in quadrature), we weight the values inversely with their variances, i.e. by Δ_i^{-2} .

(ii) *Quality weighting:* We apply a weighting W_Q which quantifies our degree of belief (over and above the estimated errors) in measurements obtained from spectra with different quality parameters. Following the discussion in §2.4, for spectra with $Q=A,B,C,D,E$ we use $W_Q=1,1,1,0.5,0$ in computing redshifts, $W_Q=1,1,0.5,0,0$ in computing dispersions, and $W_Q=1,1,0.5,0,0$ in computing linestrengths.

(iii) *Run weighting:* we also apply a run-weighting $W_R=0$ to exclude run 115, for reasons explained in §2.1; all other runs are given $W_R=1$.

The combined estimate X is thus computed from the individual measurements X_i as the weighted mean

$$X = \sum_i W_i X_i / \sum_i W_i, \quad (10)$$

where $W_i = \Delta_i^{-2} W_{Q_i} W_{R_i}$. The uncertainty in this weighted mean is computed as

$$\Delta = (\sum_i W_i)^{-1/2}. \quad (11)$$

This procedure is used to obtain combined estimates of the redshift, dispersion and linestrengths for each galaxy. We estimate the overall quality Q as the highest quality amongst the individual measurements and obtain a combined estimate of the S/N as

$$S/N = (\sum_i (S/N)_i^2 W_{Q_i} W_{R_i})^{1/2}, \quad (12)$$

using the same weightings as for the dispersions (except when the overall quality is $Q=D$, when these weightings are omitted).

Table 5 gives the combined estimates of the spectroscopic parameters for each galaxy in the EFAR sample. The version of the table presented here is abridged; the full table will be available upon publication from NASA’s Astrophysical Data Center (ADC) and from the Centre de Données astronomiques de Strasbourg (CDS). The table lists: galaxy identification number (GIN), galaxy name, cluster assignment number (CAN; see §5), and the number of spectra, redshifts, dispersions and Mgb and Mg_2 linestrengths obtained for this object; then, for each of redshift, dispersion, Mgb and Mg_2 : the combined estimate, its estimated total error (Δ) and the weighted rms error from any repeat observations (δ); finally, the combined S/N estimate and the overall quality parameter (with an asterisk if the galaxy possesses emission lines). Note that only objects with useful measurements are included; hence the lowest quality class present in this table is $Q=D$, and the 7 galaxies with only $Q=E$ spectra (GINs 123, 284, 389, 448, 599, 637, 679) in Table 3 are omitted.

The cumulative distributions of uncertainties in the combined results are shown in Figure 8, both for the entire dataset and for quality classes A, B and C separately. The error distributions can be quantitatively characterised by their 50% and 90% points, which are listed in Table 6. The overall median error in redshift is 20 km s^{-1} , the median relative errors in dispersion and Mgb are 9.1% and 7.2%, and the median error in Mg_2 is 0.015 mag. For the whole sample, and for quality classes A and B, the median errors in the combined measurements are smaller than the median errors in the individual measurements, as one expects. However for dispersion, Mgb and Mg_2 the errors are larger for quality class C and at the 90th percentile; this results from assigning a quality weighting of 0.5 to $Q=C$ when combining the individual measurements of these quantities.

The uncertainties listed in Table 5 represent the best estimates of the total errors in the parameters for each galaxy. However it must be emphasised that they are *not* independent of each other, as the run correction errors are correlated across all measurements from a run. To properly simulate the joint distribution of some parameter for the whole dataset, one must first generate realisations of

Table 5. Spectroscopic parameters for the EFAR galaxies (abridged)

(1)	(2)	(3)	(4)	(5)	(6)	(7)	(8)	(9)	(10)	(11)	(12)	(13)	(14)	(15)	(16)	(17)	(18)
GIN	Galaxy Name	CAN	N $s z \sigma b 2$	cz ... (km s ⁻¹) ...	Δcz	δcz	σ	$\Delta\sigma$	$\delta\sigma$	Mgb	Δ Mgb	δ Mgb	Mg ₂	Δ Mg ₂	δ Mg ₂	S/N	Q
							.. (km s ⁻¹)(Å).....		(mag).....				
1	A76 A	1	1 1 1 1 1	11296	53	—	262	53	—	5.20	0.57	—	0.353	0.024	—	21.4	A
2	A76 B	1	1 1 1 1 1	11317	49	—	224	49	—	4.76	0.62	—	0.326	0.024	—	18.8	B
3	A76 C	1	1 1 1 1 1	11973	51	—	217	50	—	5.17	0.70	—	0.392	0.025	—	17.8	A
4	A76 D	1	1 1 1 1 1	12184	33	—	316	150	—	6.18	1.21	—	0.326	0.041	—	10.5	C
5	A76 E	1	2 2 2 2 2	12189	14	47	184	10	23	6.26	0.18	0.09	0.295	0.010	0.018	46.7	B
6	A76 F	1	1 1 1 1 1	12371	30	—	307	85	—	5.29	0.86	—	0.331	0.028	—	17.6	B
8	A85 A	2	2 2 1 1 1	16604	35	49	290	53	—	5.14	0.61	—	0.344	0.022	—	18.7	B
9	A85 B	2	1 1 1 1 0	17349	35	—	436	47	—	5.74	0.25	—	—	—	—	37.6	A
10	A85 C	102	1 1 0 0 0	22837	71	—	—	—	—	—	—	—	—	—	—	33.9	D
11	A85 1	2	1 1 1 1 1	15112	22	—	195	19	—	3.82	0.42	—	0.253	0.018	—	25.8	B
12	A85 2	2	1 1 1 1 1	16264	31	—	294	37	—	5.86	0.37	—	0.337	0.019	—	28.3	B
13	A119 A	3	3 3 3 3 2	11459	15	17	297	15	13	5.04	0.16	0.31	0.316	0.009	0.010	56.4	A
14	A119 B	3	2 2 2 2 2	13330	20	42	278	21	10	4.90	0.22	0.21	0.358	0.010	0.011	36.5	A
15	A119 C	3	2 2 2 2 1	13500	16	11	253	17	6	5.57	0.20	0.14	0.295	0.011	—	38.5	A
16	A119 D	3	3 3 1 1 1	14982	16	9	104	18	—	3.30	0.52	—	0.151	0.023	—	14.7	C*
17	A119 E	3	2 2 2 2 1	12798	14	9	248	14	4	5.37	0.16	0.35	0.326	0.010	—	45.1	A
18	A119 F	3	2 2 2 2 1	13018	12	14	175	13	33	4.88	0.28	0.11	0.245	0.013	—	32.1	B
19	A119 G	3	2 1 1 1 0	13457	20	—	267	21	—	4.78	0.22	—	—	—	—	36.7	A
21	A119 I	3	1 1 1 1 1	13271	22	—	225	20	—	4.85	0.41	—	0.326	0.016	—	31.0	A
22	A119 J	3	1 1 1 1 0	13520	22	—	219	25	—	4.55	0.35	—	—	—	—	22.3	B
23	A119 1	103	1 1 1 1 0	4127	19	—	92	54	—	0.50	1.12	—	—	—	—	8.1	C*
24	A119 2	3	2 1 1 1 0	12346	17	—	100	20	—	5.13	0.39	—	—	—	—	20.4	B
25	J3 A	4	1 1 1 1 1	14453	34	—	333	114	—	6.25	0.77	—	0.329	0.026	—	15.2	B
26	J3 B	4	1 1 1 1 0	13519	19	—	231	16	—	4.93	0.26	—	—	—	—	39.5	A
27	J3 C	4	1 1 1 1 1	13770	23	—	163	57	—	4.33	1.26	—	0.224	0.040	—	11.2	C
28	J3 D	4	2 2 2 2 0	14610	15	258	231	13	37	5.18	0.20	0.29	—	—	—	47.6	A
31	J4 A	5	1 1 1 1 1	12074	26	—	185	75	—	5.35	1.11	—	0.387	0.043	—	9.3	C
32	J4 B	5	1 1 1 1 1	12090	33	—	302	148	—	4.11	1.56	—	0.261	0.047	—	9.4	C
33	J4 C	105	1 1 1 1 1	17154	36	—	358	48	—	6.20	0.32	—	0.355	0.019	—	30.0	A
36	A147 A	6	4 4 4 4 4	12771	11	19	244	9	12	4.88	0.13	0.14	0.289	0.007	0.008	89.9	A
37	A147 B	6	4 4 4 4 4	13119	11	15	316	10	20	4.68	0.11	0.30	0.304	0.006	0.017	104.2	A
38	A147 C	6	3 3 3 3 3	13156	13	8	247	12	7	5.22	0.15	0.22	0.305	0.008	0.007	66.8	A
39	A147 D	6	3 3 3 3 3	13444	12	2	185	9	15	4.98	0.18	0.28	0.294	0.008	0.004	67.8	A
40	A147 E	6	3 3 3 3 3	13049	10	10	176	8	7	4.58	0.14	0.12	0.267	0.007	0.002	76.1	A
41	A147 F	6	2 2 2 2 2	11922	12	5	87	10	4	3.65	0.27	0.02	0.195	0.012	0.002	37.9	B
42	A147 1	6	3 3 3 3 3	12832	11	29	148	9	3	4.35	0.16	0.09	0.252	0.008	0.013	65.8	A
43	A160 A	7	2 2 2 2 1	11401	15	3	181	17	19	3.86	0.26	0.04	0.250	0.017	—	35.1	A
44	A160 B	107	3 3 1 1 1	18258	24	17	192	21	—	6.61	0.30	—	0.289	0.022	—	26.3	B
45	A160 C	7	1 1 1 1 0	12380	34	—	412	58	—	4.61	0.37	—	—	—	—	27.8	A
46	A160 D	107	3 3 0 0 0	18271	41	84	—	—	—	—	—	—	—	—	—	36.1	D
47	A160 E	7	4 4 4 4 2	14056	13	24	226	16	12	5.01	0.23	0.26	0.293	0.017	0.014	39.2	A
48	A160 F	7	3 3 3 3 2	13657	14	16	176	18	27	5.18	0.24	0.43	0.307	0.013	0.009	33.9	A
49	A160 G	7	4 4 4 4 2	13137	13	25	196	20	22	4.82	0.25	0.39	0.293	0.015	0.056	32.4	B
50	A160 H	7	1 1 1 1 0	13589	21	—	195	23	—	5.18	0.30	—	—	—	—	21.6	A
51	A160 I	107	3 3 0 0 0	18643	41	30	—	—	—	—	—	—	—	—	—	43.9	D
52	A160 J	7	4 4 4 4 1	11254	9	13	145	10	15	2.74	0.20	0.32	0.217	0.041	—	46.1	A*
53	A160 1	107	2 2 0 0 0	18108	50	103	—	—	—	—	—	—	—	—	—	27.3	D*
54	A160 2	107	1 1 0 0 0	18201	71	—	—	—	—	—	—	—	—	—	—	21.7	D
56	A168 A	108	1 1 1 1 0	5299	19	—	265	16	—	4.35	0.26	—	—	—	—	51.7	A
57	A168 B	108	1 1 1 1 0	5253	23	—	310	25	—	5.29	0.30	—	—	—	—	43.6	A

This is an abridged version of this table; the full table will be available upon publication from NASA's Astrophysical Data Center (ADC) and from the Centre de Données astronomiques de Strasbourg (CDS). The columns of this table give: (1) galaxy identification number (GIN); (2) galaxy name; (3) the cluster assignment number (CAN); (4) the number of spectra N_s , redshifts N_z , dispersions N_σ , Mgb linestrengths N_b and Mg₂ linestrengths N_2 obtained for this object; then the combined estimate, its estimated total error (Δ) and the weighted rms error from any repeat observations (δ) for each of (5–7) redshift, (8–10) Mgb linestrength and (11–16) Mg₂ linestrength; (17) the combined S/N estimate; and (18) the overall quality parameter (with an asterisk if the galaxy possesses emission lines). Only objects with useful measurements are included; hence the lowest quality class present in this table is $Q=D$, and the 7 galaxies with only $Q=E$ spectra (GINs 123, 284, 389, 448, 599, 637, 679) are omitted.

Table 6. The distribution of errors per galaxy

Q	Δcz (km/s)		$\Delta\sigma/\sigma$		$\Delta Mgb/Mgb$		ΔMg_2 (mag)	
	50%	90%	50%	90%	50%	90%	50%	90%
All	20	36	0.091	0.240	0.072	0.188	0.015	0.032
A	17	30	0.067	0.161	0.053	0.120	0.012	0.023
B	23	44	0.118	0.270	0.103	0.194	0.018	0.033
C	24	47	0.220	0.507	0.180	0.425	0.030	0.048

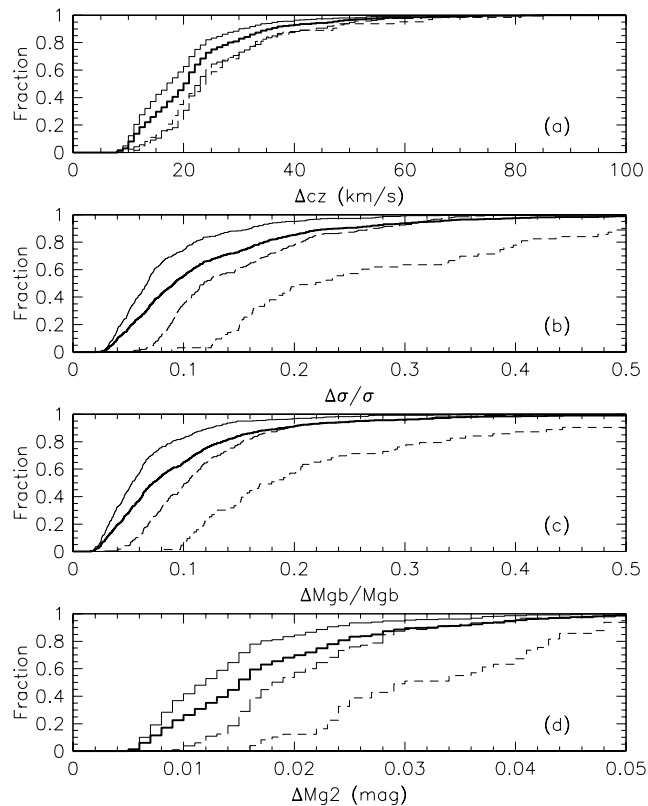


Figure 8. The cumulative distributions of the total estimated errors in the combined measurements of redshift, velocity dispersion, Mgb and Mg₂ for each galaxy. The distributions for quality classes A, B and C are shown as full, long-dashed and short-dashed lines respectively; the overall distribution is shown as the thick full line. (a) The distribution of combined errors in cz ; (b) combined relative errors in σ ; (c) combined relative errors in Mgb; (d) combined errors in Mg₂.

the run correction errors (drawn from Gaussians with standard deviations given by the uncertainties listed in Table 2) and the individual measurement errors (drawn from Gaussians with standard deviations given by the uncertainties listed Table 3). For each individual measurement, one must add the realisation of its measurement error and the realisation of the appropriate run correction error (the same for all measurements in a given run) to the measured value of the parameter. The resulting realisations of the individual measurements are finally combined using the recipe described above to yield a realisation of the value of the parameter for each galaxy in the dataset.

The distributions of redshift, velocity dispersion, Mgb and Mg₂ for the galaxies in the EFAR sample are displayed in Figure 9. The galaxies for which we measured velocity dispersions are only a subset of our sample of programme

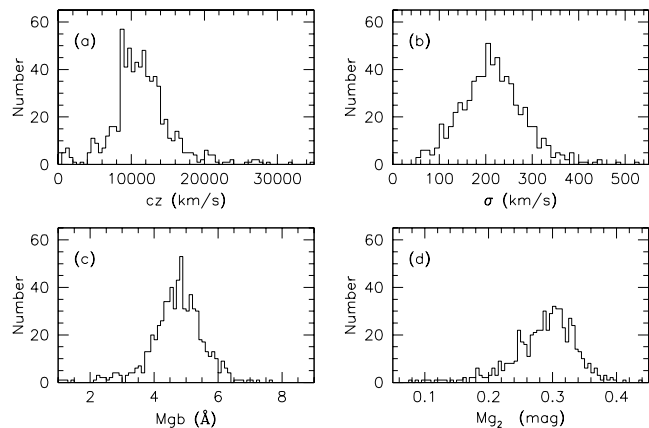


Figure 9. The distributions of (a) redshift, (b) velocity dispersion, (c) Mgb linestrength, and (d) Mg₂ linestrength for the galaxies in the EFAR sample.

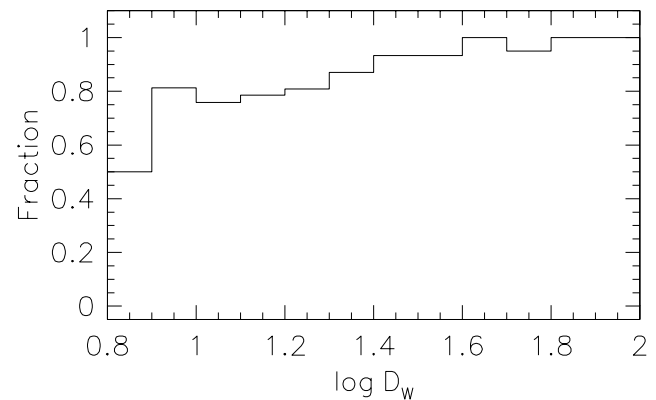


Figure 10. The fraction of programme objects for which we measured a velocity dispersion as a function of the logarithm of the selection diameter D_W (in arcsec).

galaxies (629/743), and represent a refinement of the sample selection criteria. Figure 10 shows the fraction of programme galaxies with measured dispersions as a function of the galaxy diameter D_W on which the selection function of the programme galaxy sample is defined. There is a steady decline in the fraction of the sample for which usable dispersions were measured, from 100% for the largest galaxies (with $D_W \gtrsim 40$ arcsec) to about 75% for the smallest (with $8 \text{ arcsec} \lesssim D_W \lesssim 15 \text{ arcsec}$; there are only 3 programme galaxies with $D_W < 8 \text{ arcsec}$). This additional selection effect must be allowed for when determining Fundamental Plane distances.

4.3 Internal and External Comparisons

One of the strengths of our spectroscopic sample is the high fraction of objects with repeat observations: there are 375 galaxies with a single dispersion measurement, 160 with two measurements and 141 with three or more measurements. Figure 11 shows the cumulative distributions of rms errors in redshift, dispersion, Mgb and Mg₂ obtained from these repeat observations. The detailed internal comparisons made possible by these repeat measurements have been used to

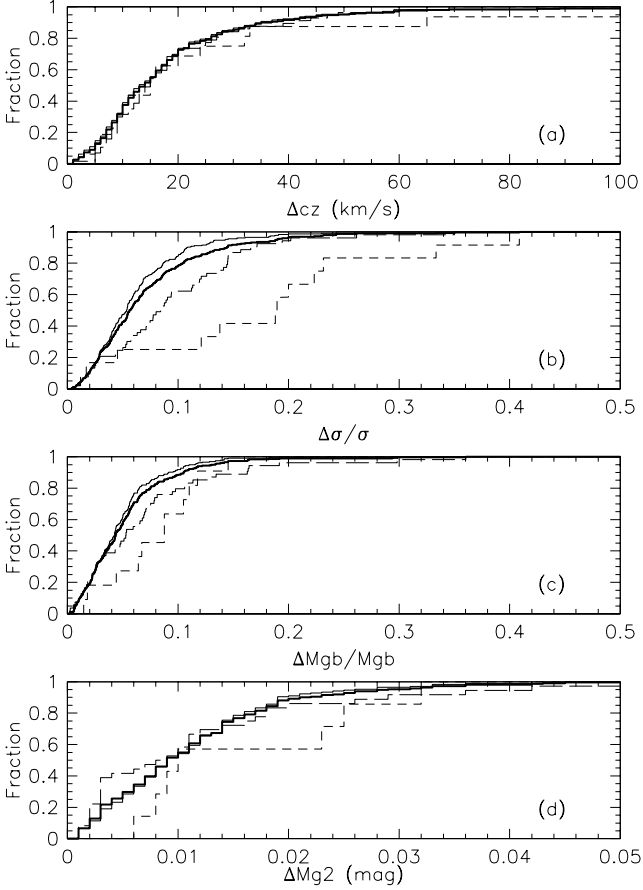


Figure 11. The cumulative distributions of the rms errors from repeat measurements of redshift, velocity dispersion, Mgb and Mg₂. The distributions for spectral types A, B and C are shown as full, long-dashed and short-dashed lines respectively; the overall distribution is shown as the thick full line. (a) The distribution of rms errors in cz in km s^{-1} ; (b) relative rms errors in σ ; (c) relative rms errors in Mgb; (d) rms errors in Mg₂.

establish the run corrections (§3.5) and to calibrate the estimated errors (§3.6). The latter process ensured that the estimated errors were statistically consistent with the rms errors of the repeat measurements.

We also make external comparisons of our measurements with the work of other authors. The EFAR redshifts are compared in Figure 12 with redshifts given in the literature by the 7 Samurai (Davies et al. 1987), Dressler & Shectman (1988), Beers et al. (1991), Malumuth et al. (1992), Zabludoff et al. (1993), Colless & Dunn (1996) and Lucey et al. (1997). Only 11 of the 256 comparisons give redshift differences greater than 300 km s^{-1} : in 6 cases the EFAR redshift is confirmed either by repeat measurements or other published measurements; in the remaining 5 cases the identification of the galaxy in question is uncertain in the literature. For the 245 cases where the redshift difference is less than 300 km s^{-1} , there is no significant velocity zero-point error and the rms scatter is 85 km s^{-1} . Since our repeat measurements show much smaller errors (90% are less than 36 km s^{-1}), most of this scatter must arise in the literature data, some of which were taken at lower resolution or S/N than our data.

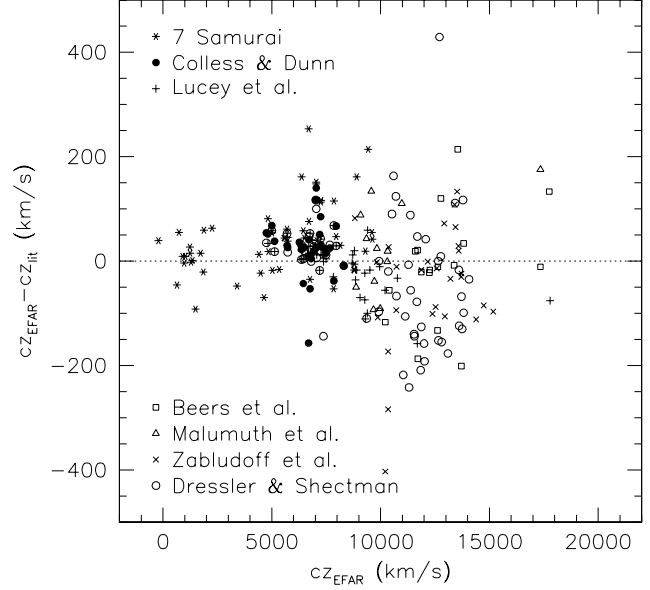


Figure 12. Differences between EFAR redshifts and those from various sources in the literature.

Figure 13 compares the EFAR dispersions with published dispersions from the work of the 7 Samurai (Davies et al. 1987), Guzmán (1993), Jørgensen et al. (1995) and Lucey et al. (1997), and the compilation of earlier measurements by Whitmore et al. (1985). Note that we do not compare to the more recent compilation by McElroy (1995), since its overlap with our sample is essentially just the sum of above sources. The mean differences, $\Delta = \log \sigma_{EFAR} - \log \sigma_{lit}$, and their standard errors are indicated on the figure; none of these scale differences is larger than 6% and in fact all five comparisons are consistent with zero scale error at the 2σ level or better. The rms scatter in these comparisons is significantly greater than the errors in our dispersion measurements, implying that in general the literature measurements have larger errors and/or that there are unaccounted-for uncertainties in the comparison.

We determine the zeropoint calibration of our linestrength measurements with respect to the Lick system (see §3.2) by comparing our Mg b' and Mg₂ linestrengths to measurements for the same galaxies given by Trager et al. (1998). We find that slightly different calibrations are needed for objects with different redshifts, the result of slight variations in the non-linear continuum shape as the spectra are redshifted with respect to the instrument response and the sky background (see §3.2). Good agreement with Trager et al. is obtained if we use different zeropoints for galaxies with redshifts above and below $cz=3000 \text{ km s}^{-1}$ (although there are no objects in the comparison at $cz>10000 \text{ km s}^{-1}$). Excluding a few outliers, we find weighted mean differences between the EFAR and Trager et al. linestrengths of $\langle \Delta \text{Mgb}' \rangle = -0.022 \text{ mag}$ and $\langle \Delta \text{Mg}_2 \rangle = -0.083 \text{ mag}$ for $cz < 3000 \text{ km s}^{-1}$, and $\langle \Delta \text{Mgb}' \rangle = -0.008 \text{ mag}$ and $\langle \Delta \text{Mg}_2 \rangle = -0.028 \text{ mag}$ for $cz > 3000 \text{ km s}^{-1}$. Subtracting these zeropoint corrections gives the final, fully-corrected, linestrength measurements as listed in Tables 3 & 5. Figures 14 & 15 show the residual differences between the EFAR and Trager et al. linestrength

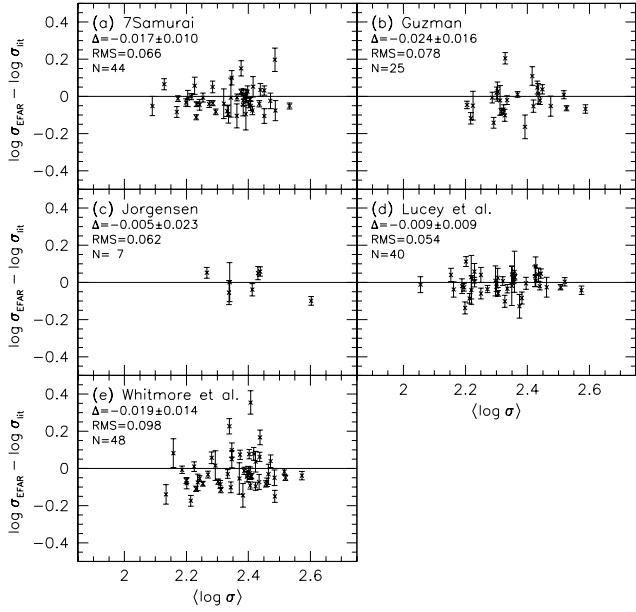


Figure 13. Comparisons of EFAR dispersions with those from various sources in the literature: (a) Davies et al. (1987), (b) Guzmán (1993), (c) Jørgensen (1997), (d) Lucey et al. (1997), and (e) Whitmore et al. (1985). In each case the mean difference, $\Delta = (\log \sigma_{EFAR} - \log \sigma_{lit})$, and its standard error are indicated, along with the rms scatter and the number of galaxies in the comparison.

measurements after applying these zeropoint corrections. The rms scatter is 0.019 mag in Mgb' for the 41 objects in common, and 0.023 mag in Mg_2 for the 24 objects in common. There is no statistically significant trend with linestrength, velocity dispersion or redshift remaining in the residuals after these zeropoint corrections are applied.

Figure 16 compares our calibrated Mg_2 linestrengths to those obtained in A2199, A2634 and Coma by Lucey et al. (1997). The overall agreement for the 36 objects in common is very good, with a statistically non-significant zeropoint offset and an rms scatter of 0.029 mag, similar to that found in the comparison with Trager et al.

The relation between the measured Mgb' and Mg_2 linestrengths for all the galaxies in the EFAR sample is shown in Figure 17. We fit this relation using a maximum likelihood technique which accounts for both measurement errors and selection effects (Saglia et al. 1998, in preparation; Paper VI). We find

$$Mg_2 = 1.94Mgb' - 0.05, \quad (13)$$

with a perpendicular rms residual of 0.019 mag (corresponding to an rms of 0.041 mag in Mg_2 , or 0.021 mag in Mgb'). The relation is the same if we fit ellipticals, E/S0s, cDs or spirals separately. This relation is similar to those derived by Burstein et al. (1984) and Jørgensen (1997). We can therefore use Mgb' as a predictor of Mg_2 (albeit with larger uncertainties) for those cases where Mg_2 cannot be measured directly.

Also shown in Figure 17 is the predicted relation between Mgb' and Mg_2 as a function of age and metallicity given by Worthey (1994). His models correctly predict the slope of the relation, but are offset by -0.025 mag in Mgb' (or

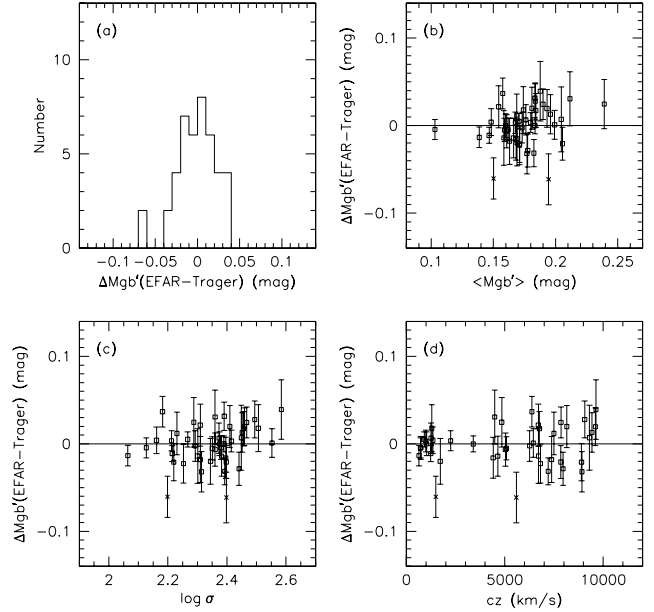


Figure 14. The residual differences in Mgb' linestrengths from EFAR and Trager et al. (1998) after applying the zeropoint corrections discussed in the text: (a) the distribution of residuals; (b) the residuals as a function of Mgb' ; (c) the residuals as a function of $\log \sigma$; (d) the residuals as a function of redshift. Outliers excluded from the determination of the zeropoint corrections are shown as crosses.

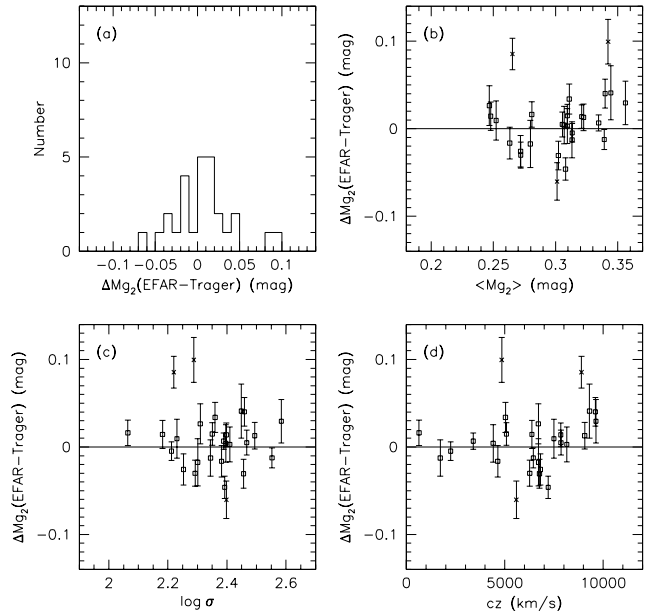


Figure 15. The residual differences in Mg_2 linestrengths from EFAR and Trager et al. (1998) after applying the zeropoint corrections discussed in the text: (a) the distribution of residuals; (b) the residuals as a function of Mg_2 ; (c) the residuals as a function of $\log \sigma$; (d) the residuals as a function of redshift. Outliers excluded from the determination of the zeropoint corrections are shown as crosses.

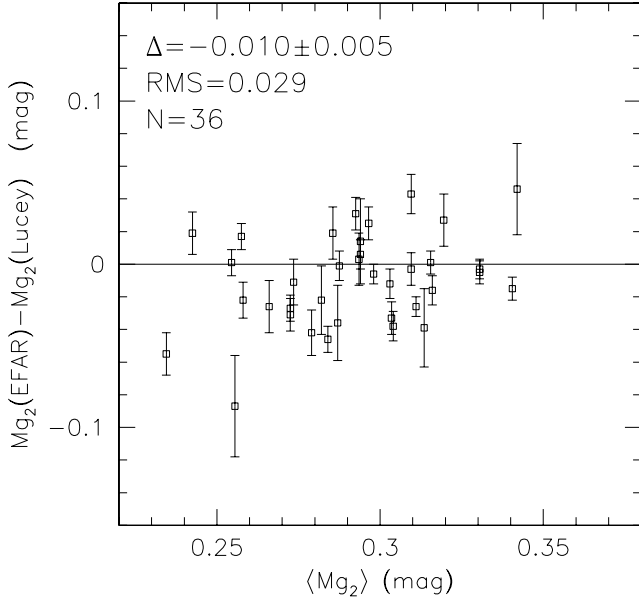


Figure 16. Comparisons of Mg_2 linestrengths obtained by EFAR and Lucey et al. (1997). The mean difference, $\Delta = Mg_2(\text{EFAR}) - Mg_2(\text{Lucey})$, and its standard error are indicated, along with the rms scatter and the number of galaxies in the comparison.

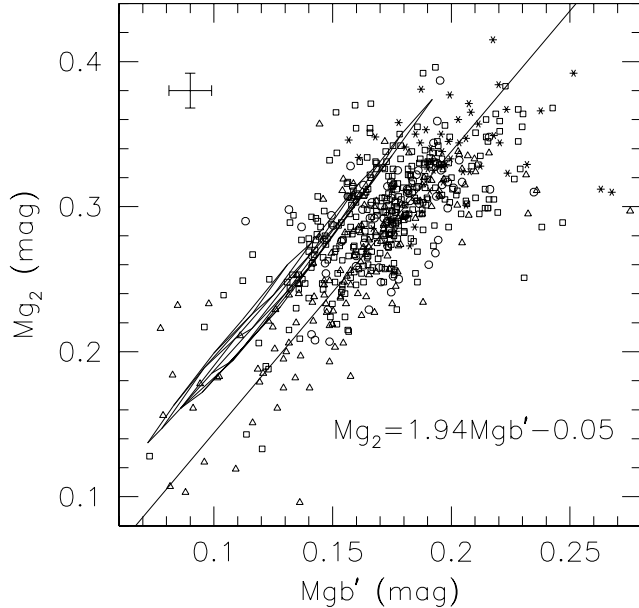


Figure 17. The relation between Mgb' and Mg_2 and its maximum likelihood fit. Ellipticals are marked by circles, E/S0s by squares, cDs by asterisks and spirals by triangles. Typical estimated errors are shown in the top left corner. The relation between Mgb' and Mg_2 as a function of age and metallicity, as predicted by Worthey (1994), is shown as the grid lying parallel to, but offset from, the data.

by $+0.05$ mag in Mg_2), indicating a difference in the model's zeropoint calibration for one or both indices.

5 CLUSTER ASSIGNMENTS

The correct assignment of galaxies to clusters (or groups) is crucial to obtaining reliable redshifts and distances for the EFAR cluster sample. We also need to increase the precision of the cluster redshifts in order to minimise uncertainties in the clusters' peculiar velocities. To achieve these goals we merged the EFAR redshifts with redshifts for all galaxies in ZCAT (Huchra et al., 1992; version of 1997 May 29) which lie within $3 h^{-1}$ Mpc (2 Abell radii) of each nominal EFAR cluster centre (see Table 1 of Paper I). We then examined the redshift distributions of the combined sample in order to distinguish groups, clusters and field galaxies along the line of sight to a nominal EFAR 'cluster'. We also considered the distribution of galaxies on the sky before assigning the EFAR galaxies to specific groupings.

The results of this process are shown in Figure 18, which shows the redshift distributions of galaxies within $3 h^{-1}$ Mpc around each of the nominal EFAR clusters (labelled by their cluster ID number, CID; see Paper I) and the adopted groupings in redshift space. Note that CID=81 (A2593-S) does not appear since it was merged with CID=80 (A2593-N)—see below. Each EFAR galaxy was assigned to one of these groupings and given a cluster assignment number (CAN), listed in Table 5. The main grouping along the line of sight has a CAN which is simply the original two-digit CID; other groupings have CANs with a distinguishing third leading digit. The groupings (which we will hereafter call clusters regardless of their size) are labelled by their CANs in Figure 18, which also shows the boundaries of each cluster in redshift space. The last two digits of each galaxy's CAN is its CID, apart from 41 galaxies which were reassigned to other neighbouring clusters: two galaxies in CID=33 were reassigned to CAN=34 (GINs 254, 255); two galaxies in CID=34 were reassigned to CAN=33 (GINs 263, 264); five galaxies in CID=35 were reassigned to CAN=36 (GINs 270, 274, 275, 281, 282); fourteen galaxies in CID=36 were reassigned to CAN=35 (GINs 285–292, 295–297, 299–301), one galaxy in CID=47 was reassigned to CAN=50 (GIN 406); three galaxies in CID=59 and two in CID=61 were reassigned to CAN=53 (GINs 514, 517, 527, 536, 537); five galaxies with CID=69 were reassigned to CAN=70 (GINs 617, 618, 619, 622, 623); and all seven galaxies with CID=81 were reassigned to CAN=80 (GINs 709–715).

Table 7 lists, for each CAN, the number of EFAR galaxies, the number of EFAR+ZCAT galaxies, and the mean redshift, its standard error (taken to the error in the redshift for clusters with only one member) and the velocity dispersion. These quantities are computed both from the EFAR sample and from the EFAR+ZCAT sample. In many of the clusters the EFAR sample is greatly supplemented by the ZCAT galaxies, leading to much-improved estimates of the mean cluster redshift: using EFAR galaxies only the median uncertainty in the mean cluster redshift (for clusters with more than one member) is 177 km s^{-1} ; with EFAR+ZCAT galaxies the median uncertainty is reduced to 133 km s^{-1} .

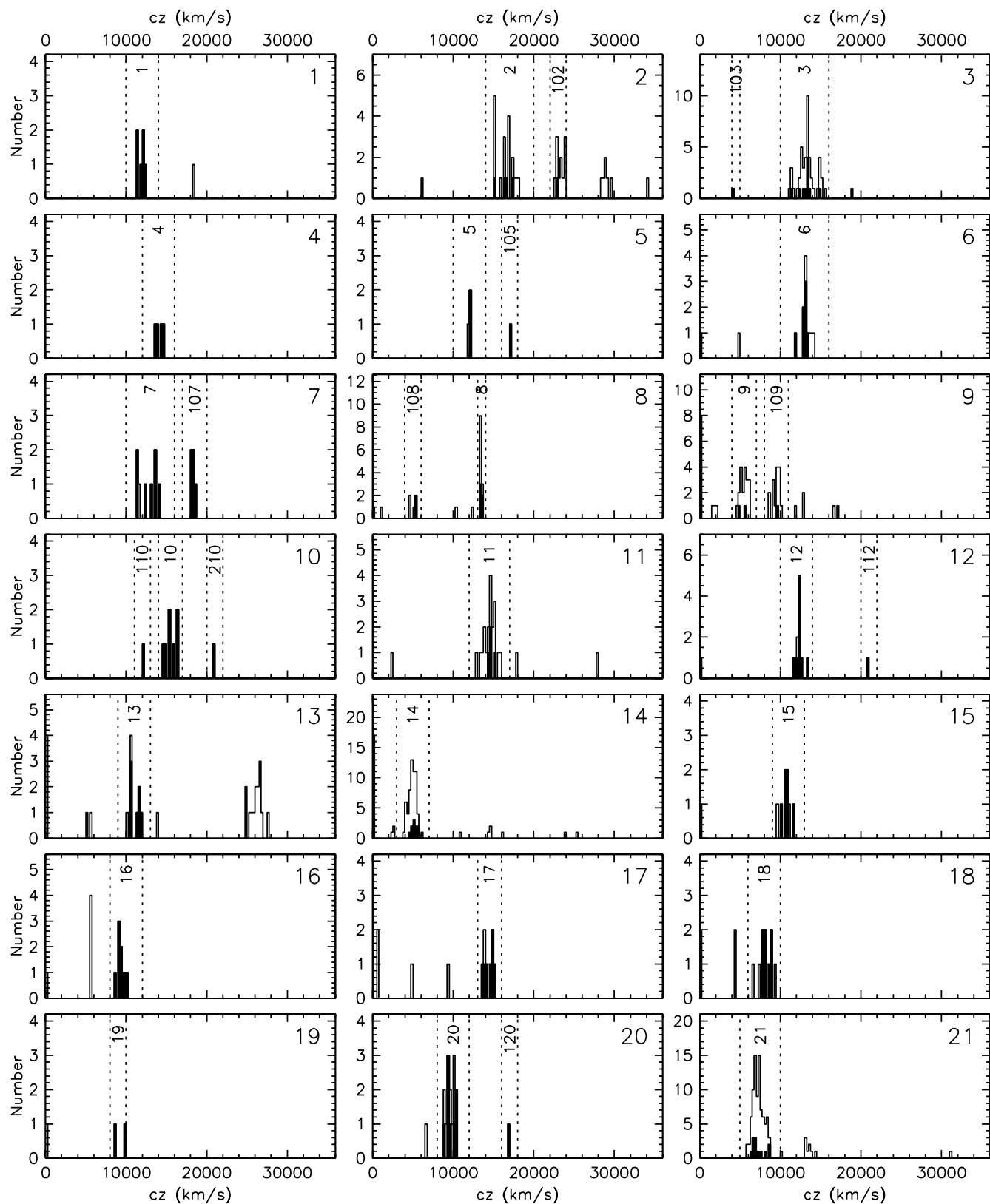
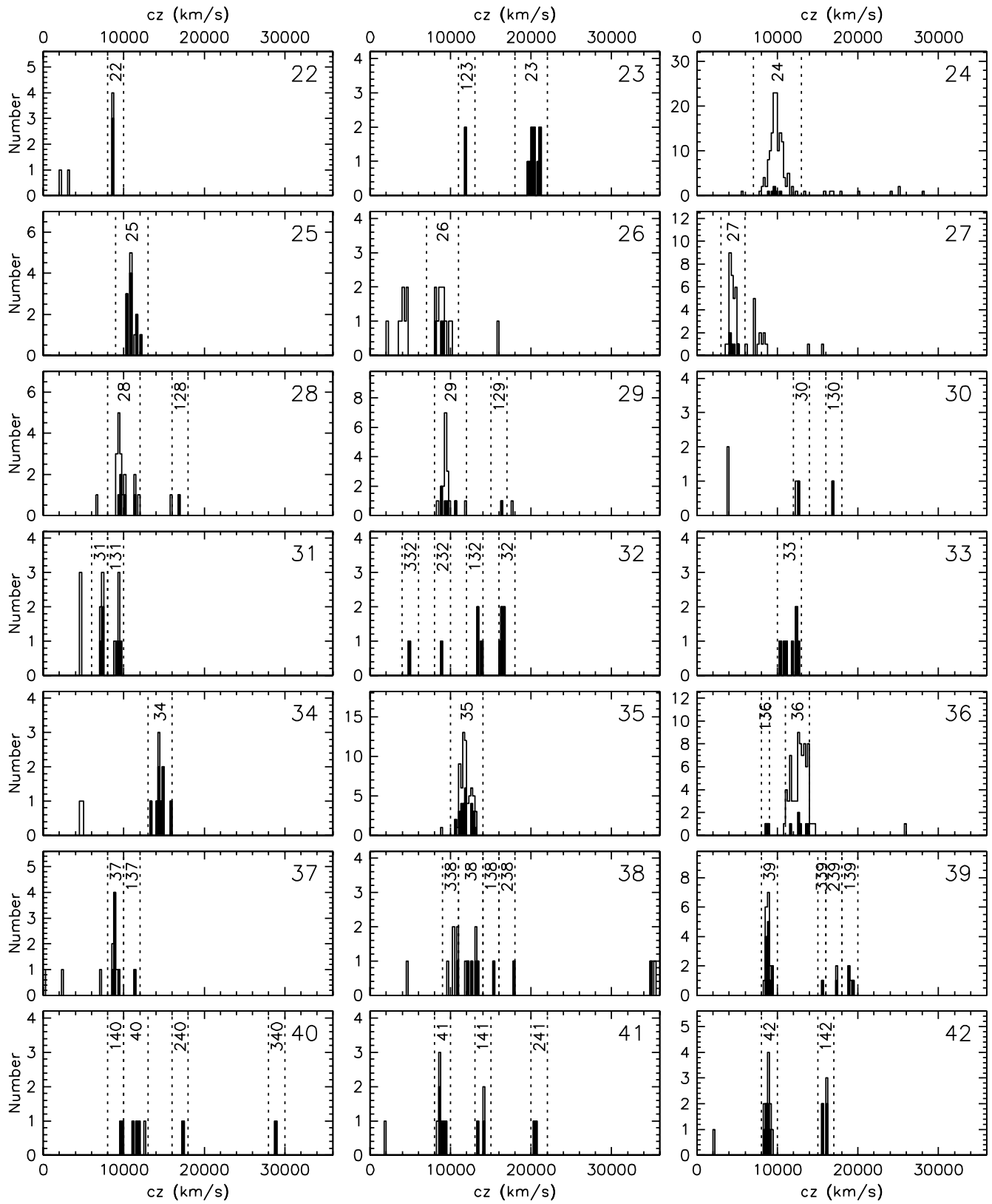


Figure 18. The redshift distributions of galaxies within $3h^{-1}$ Mpc of each nominal EFAR cluster using the EFAR and ZCAT data. Each distribution is labelled at top right by the nominal cluster ID number (CID). The solid histogram shows the distribution of EFAR galaxies; the open histogram shows the extra ZCAT galaxies. The groupings adopted have boundaries in redshift marked by dotted lines and are labelled by their cluster assignment number (CAN). Clusters without numbers and boundaries contain no EFAR galaxies.

Figure 18. (*ctd*)

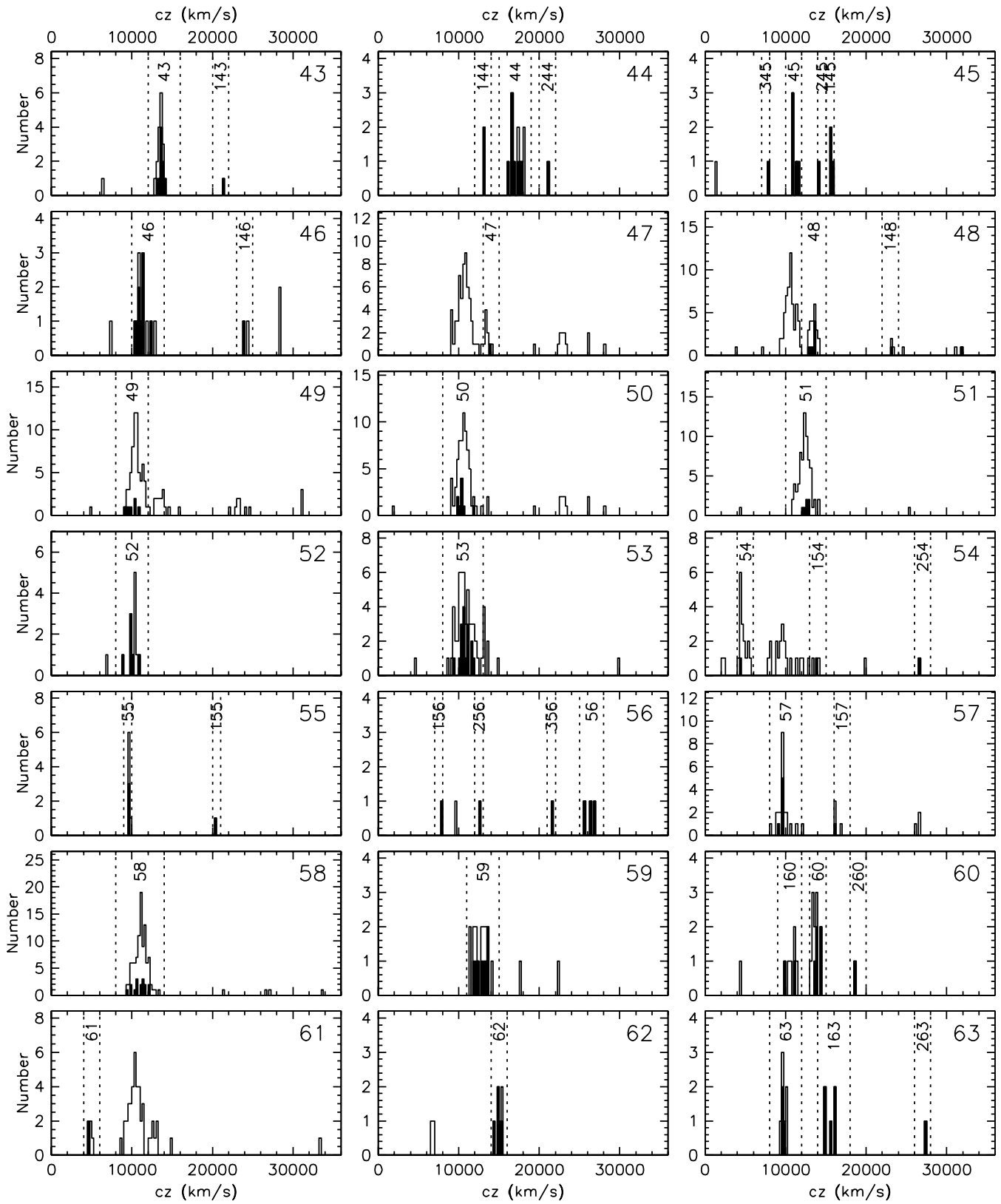


Figure 18. (ctd)

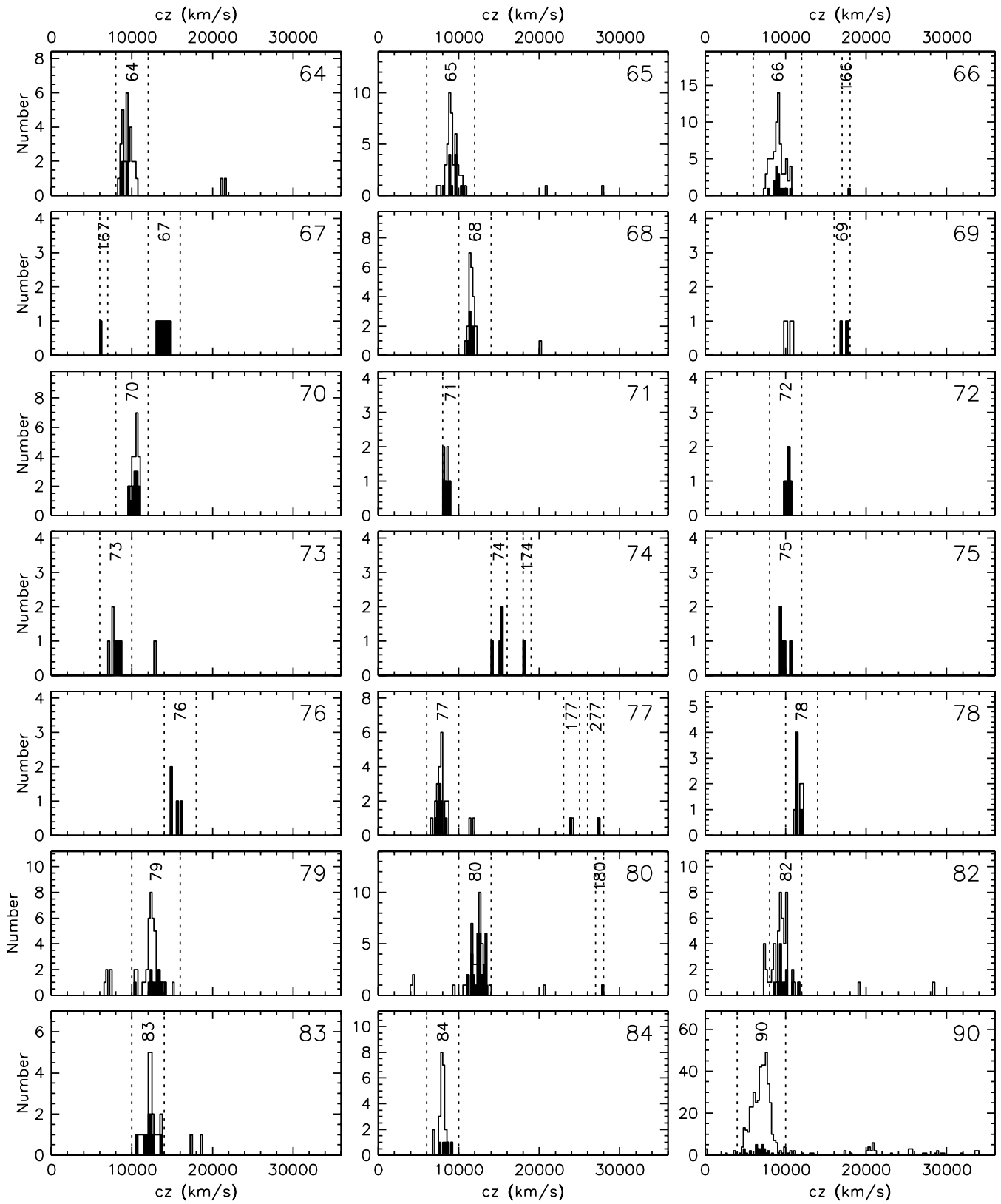


Figure 18. (ctd)

Table 7. Cluster mean redshifts and velocity dispersions

..... EFAR EFAR+ZCAT EFAR EFAR+ZCAT		
CAN	N	$\langle cz \rangle$	σ	N	$\langle cz \rangle$	σ	CAN	N	$\langle cz \rangle$	σ	N	$\langle cz \rangle$	σ
1	6	11888 ± 191	468	6	11888 ± 191	468	241	2	20440 ± 94	134	2	20440 ± 94	134
2	4	16332 ± 466	931	19	16454 ± 227	991	42	6	8783 ± 114	280	11	8856 ± 93	309
102	1	22837 ± 71	—	11	23340 ± 134	444	142	4	15863 ± 146	292	5	15917 ± 125	280
3	10	13168 ± 287	907	45	13280 ± 158	1060	43	9	13667 ± 82	246	17	13536 ± 81	332
103	1	4127 ± 18	—	1	4127 ± 18	—	143	1	21438 ± 20	—	1	21438 ± 20	—
4	4	14090 ± 263	527	4	14090 ± 263	527	44	8	16950 ± 191	539	11	17184 ± 191	633
5	2	12082 ± 8	11	3	11994 ± 88	153	144	2	13190 ± 23	33	2	13190 ± 23	33
105	1	17154 ± 30	—	1	17154 ± 30	—	244	1	21199 ± 64	—	1	21199 ± 64	—
6	7	12899 ± 183	484	11	13193 ± 177	588	45	5	11123 ± 143	320	5	11123 ± 143	320
7	7	12782 ± 425	1123	8	12625 ± 400	1131	145	3	15757 ± 109	188	3	15757 ± 109	188
107	5	18296 ± 91	204	5	18296 ± 91	204	245	1	14024 ± 39	—	1	14024 ± 39	—
8	5	13466 ± 49	109	12	13414 ± 33	116	345	1	7789 ± 36	—	1	7789 ± 36	—
108	2	5276 ± 23	33	5	5000 ± 136	303	46	9	11136 ± 197	591	12	11321 ± 208	719
9	2	5212 ± 376	531	19	5482 ± 103	447	146	1	23945 ± 21	—	2	24166 ± 221	313
109	1	9599 ± 22	—	15	9473 ± 126	486	47	1	13876 ± 26	—	9	13576 ± 113	338
10	7	15546 ± 270	715	7	15546 ± 270	715	48	7	13466 ± 114	302	22	13455 ± 78	364
110	1	12206 ± 50	—	1	12206 ± 50	—	148	1	23099 ± 71	—	3	23233 ± 134	231
210	1	20957 ± 12	—	1	20957 ± 12	—	49	7	9944 ± 247	653	64	10528 ± 80	640
11	4	14747 ± 163	325	19	14499 ± 179	782	50	9	10427 ± 193	580	67	10548 ± 89	730
12	10	12342 ± 142	448	11	12315 ± 131	435	51	6	12593 ± 127	312	69	12353 ± 84	699
112	1	20993 ± 41	—	1	20993 ± 41	—	52	6	9982 ± 262	642	12	10215 ± 146	504
13	8	11074 ± 213	603	10	10944 ± 191	605	53	16	10786 ± 149	598	49	10675 ± 131	917
14	10	5145 ± 100	317	59	4935 ± 61	471	54	1	4410 ± 18	—	16	4699 ± 113	452
15	6	10725 ± 204	499	8	10655 ± 214	606	154	1	13830 ± 20	—	3	13818 ± 212	367
16	9	9376 ± 161	484	9	9376 ± 161	484	254	1	26612 ± 73	—	1	26612 ± 73	—
17	7	14417 ± 196	519	9	14355 ± 163	490	55	3	9635 ± 39	68	7	9636 ± 29	77
18	7	8353 ± 169	448	11	8206 ± 232	770	155	1	20285 ± 29	—	1	20285 ± 29	—
19	2	9256 ± 511	723	2	9256 ± 511	723	56	3	26280 ± 339	587	3	26280 ± 339	587
20	8	9676 ± 172	486	14	9663 ± 126	472	156	1	7955 ± 15	—	1	7955 ± 15	—
120	1	16841 ± 15	—	1	16841 ± 15	—	256	1	12730 ± 18	—	1	12730 ± 18	—
21	13	7241 ± 210	757	86	7253 ± 72	663	356	1	21558 ± 71	—	1	21558 ± 71	—
22	3	8666 ± 28	48	4	8649 ± 26	53	57	6	9520 ± 107	263	22	9582 ± 132	617
23	9	20400 ± 188	565	9	20400 ± 188	565	157	1	16075 ± 45	—	4	16237 ± 192	384
123	2	11852 ± 34	49	2	11852 ± 34	49	58	16	10943 ± 197	789	99	11106 ± 79	781
24	6	9651 ± 204	499	137	9854 ± 66	776	59	8	12864 ± 242	683	16	12693 ± 215	862
25	10	10999 ± 204	646	12	11021 ± 172	596	60	5	13993 ± 142	318	11	13707 ± 119	393
26	3	8677 ± 297	514	12	8937 ± 189	653	160	2	10474 ± 651	921	6	10730 ± 223	547
27	5	4540 ± 188	420	30	4436 ± 65	355	260	1	18545 ± 26	—	1	18545 ± 26	—
28	5	10030 ± 363	813	17	9884 ± 208	857	61	2	4742 ± 16	11	5	4878 ± 90	202
128	1	16920 ± 27	—	1	16920 ± 27	—	62	5	14918 ± 167	373	6	14991 ± 154	378
29	5	9492 ± 339	759	18	9528 ± 181	769	63	3	9699 ± 92	159	7	9777 ± 116	306
129	1	16483 ± 18	—	1	16483 ± 18	—	163	5	15563 ± 273	610	5	15563 ± 273	610
30	1	12711 ± 19	—	2	12576 ± 135	191	263	1	27486 ± 71	—	1	27486 ± 71	—
130	1	16760 ± 14	—	1	16760 ± 14	—	64	5	9062 ± 154	345	28	9423 ± 113	598
31	3	7288 ± 47	81	5	7289 ± 31	69	65	11	9223 ± 171	568	46	9137 ± 97	659
131	3	9384 ± 171	296	6	9299 ± 102	250	66	15	9156 ± 178	689	73	9014 ± 93	796
32	5	16416 ± 94	210	5	16416 ± 94	210	166	1	17795 ± 44	—	1	17795 ± 44	—
132	3	13499 ± 144	250	3	13499 ± 144	250	67	7	13876 ± 215	570	7	13876 ± 215	570
232	1	8926 ± 9	—	1	8926 ± 9	—	167	1	6086 ± 12	—	1	6086 ± 12	—
332	1	4758 ± 9	—	1	4758 ± 9	—	68	8	11514 ± 97	273	22	11547 ± 67	316
33	7	11652 ± 340	899	7	11652 ± 340	899	69	2	17344 ± 403	570	2	17344 ± 403	570
34	8	14498 ± 265	749	9	14488 ± 234	702	70	13	10320 ± 109	392	23	10396 ± 78	376
35	27	11834 ± 133	694	66	11866 ± 78	630	71	4	8465 ± 147	294	6	8442 ± 113	278
36	6	12861 ± 309	757	69	12732 ± 101	837	72	5	10311 ± 136	305	5	10311 ± 136	305
136	2	8764 ± 234	331	2	8764 ± 234	331	73	3	8121 ± 176	305	7	7935 ± 194	514
37	6	8888 ± 81	199	8	8866 ± 82	231	74	4	14965 ± 267	534	4	14965 ± 267	534
137	1	11399 ± 18	—	1	11399 ± 18	—	174	1	18187 ± 36	—	1	18187 ± 36	—
38	4	12788 ± 280	559	6	12695 ± 252	616	75	5	9784 ± 233	521	5	9784 ± 233	521
138	1	15405 ± 16	—	1	15405 ± 16	—	76	4	15365 ± 320	640	4	15365 ± 320	640
238	1	17845 ± 27	—	1	17845 ± 27	—	77	9	7639 ± 124	373	20	7728 ± 112	502
338	1	10873 ± 35	—	5	10438 ± 236	528	177	1	23926 ± 12	—	2	23992 ± 66	93
39	12	8882 ± 69	238	18	8832 ± 61	257	277	1	27282 ± 13	—	1	27282 ± 13	—
139	3	19044 ± 183	317	4	19076 ± 133	266	78	6	11504 ± 133	327	9	11571 ± 136	408
239	1	17438 ± 55	—	2	17443 ± 5	7	79	10	12692 ± 328	1036	40	12441 ± 149	944
339	1	15651 ± 30	—	1	15651 ± 30	—	80	24	12331 ± 133	649	48	12399 ± 107	740
40	3	11612 ± 217	376	4	11846 ± 280	560	180	1	27823 ± 8	—	1	27823 ± 8	—
140	2	9806 ± 160	226	2	9806 ± 160	226	82	12	9771 ± 238	824	43	9573 ± 113	741
240	1	17291 ± 26	—	1	17291 ± 26	—	83	9	12157 ± 253	759	23	12252 ± 156	748
340	1	28973 ± 28	—	1	28973 ± 28	—	84	5	8345 ± 224	500	24	7962 ± 90	442
41	5	8973 ± 135	303	7	8848 ± 127	335	90	29	6663 ± 172	924	435	6942 ± 50	1034
141	2	13685 ± 405	573	3	13794 ± 258	447							

6 CONCLUSIONS

We have described the observations, reductions, and analysis of 1319 spectra of 714 early-type galaxies studied as part of the EFAR project. We have obtained redshifts for 706 galaxies, velocity dispersions and *Mgb* linestrengths for 676 galaxies, and Mg_2 linestrengths for 582 galaxies. Although obtained in 33 observing runs spanning seven years and 10 different telescopes, we have applied uniform procedures to derive the spectroscopic parameters and brought all the measurements of each parameter onto a standard system which we ensure is internally consistent through comparisons of the large numbers of repeat measurements, and externally consistent through comparisons with published data. We have performed detailed simulations to estimate measurement errors and calibrated these error estimates using the repeat observations.

The fully-corrected measurements of each parameter from the individual spectra are given in Table 3; the final parameters for 706 galaxies, computed as the appropriately-weighted means of the individual measurements, are listed in Table 5. The median estimated errors in the combined measurements (including measurement errors and run correction uncertainties) are $\Delta cz = 20 \text{ km s}^{-1}$, $\Delta\sigma/\sigma = 9.1\%$ (i.e. $\Delta \log \sigma = 0.040 \text{ dex}$), $\Delta Mgb/Mgb = 7.2\%$ (i.e. $\Delta Mgb' = 0.013 \text{ mag}$) and $\Delta Mg_2 = 0.015 \text{ mag}$. Comparisons with redshifts and dispersions from the literature show no systematic errors. The linestrengths required only small zeropoint corrections to bring them onto the Lick system.

We have assigned galaxies to physical clusters (as opposed to apparent projected clusters) by examining the line-of-sight velocity distributions based on EFAR and ZCAT redshifts, together with the projected distributions on the sky. We derive mean redshifts for these physical clusters, which will be used in estimating distances and peculiar velocities, and also velocity dispersions, which will be used to test for trends in the galaxy population with cluster mass or local environment.

The results presented here comprise the largest single set of velocity dispersions and linestrengths for early-type galaxies published to date. These data will be used in combination with the sample selection criteria of Wegner et al. (1996, Paper I) and the photometric data of Saglia et al. (1997, Paper III) to analyse the properties and peculiar motions of early-type galaxies in the two distant regions studied by the EFAR project.

ACKNOWLEDGEMENTS

We gratefully acknowledge all the observatories which supported this project: MMC, RKM, RLD and DB were Visiting Astronomers at Kitt Peak National Observatory, while GB, RLD and RKM were Visiting Astronomers at Cerro Tololo Inter-American Observatory—both observatories are operated by AURA, Inc. for the National Science Foundation; GW and DB used MDM Observatory, operated by the University of Michigan, Dartmouth College and the Massachusetts Institute of Technology; DB and RKM used the Multiple Mirror Telescope, jointly operated by the Smithsonian Astrophysical Observatory and Steward Observatory; RPS used facilities at Calar Alto (Centro Astrofísico His-

pano Alemanno) and La Silla (ESO); MMC observed at Sidling Spring (MSSSO); MMC, RLD, RPS and GB used the telescopes of La Palma Observatory. We thank the many support staff at these observatories who assisted us with our observations. We thank S. Sakai for doing one observing run. We also thank the SMAC team for providing comparison data prior to publication, and Mike Hudson for helpful discussions.

We also gratefully acknowledge the financial support provided by various funding agencies: GW was supported by the SERC and Wadham College during a year's stay in Oxford, and by the Alexander von Humboldt-Stiftung during a visit to the Ruhr-Universität in Bochum; MMC acknowledges the support of a Lindemann Fellowship, DIST Collaborative Research Grants and an Australian Academy of Science/Royal Society Exchange Program Fellowship; RPS was supported by DFG grants SFB 318 and 375. This work was partially supported by NSF Grant AST90-16930 to DB, AST90-17048 and AST93-47714 to GW, and AST90-20864 to RKM. The entire collaboration benefitted from NATO Collaborative Research Grant 900159 and from the hospitality and financial support of Dartmouth College, Oxford University, the University of Durham and Arizona State University. Support was also received from PPARC visitors grants to Oxford and Durham Universities and a PPARC rolling grant 'Extragalactic Astronomy and Cosmology in Durham 1994-98'.

REFERENCES

- Baggley G., 1996, PhD thesis, University of Oxford
 Beers T.C., Forman W., Huchra J.P., Jones C., Gebhardt K., 1991, *AJ*, 102, 1581
 Burstein D., Faber S.M., Gaskell C.M., Krumm N., 1984, *ApJ*, 287, 586
 Colless M.M., 1987, PhD thesis, University of Cambridge
 Colless M.M., Dunn A.M., 1996, *ApJ*, 458, 435
 Colless M.M., Burstein D., Davies R.L., McMahan R., Saglia R.P., Wegner G., 1998, *MNRAS*, in press (Paper V)
 Colless M.M., Burstein D., Wegner G., Saglia R.P., McMahan R., Davies R.L., Bertschinger E., Baggley G., 1993, *MNRAS*, 262, 475
 Davies R.L., Burstein D., Dressler A., Faber S.M., Lynden-Bell D., Terlevich R., Wegner G., 1987, *ApJS*, 64, 581
 Dressler A., Shectman S.A., 1988, *AJ*, 95, 284
 Faber S.M., Jackson R.E., 1976, *ApJ*, 204, 668
 González J.J., 1993, PhD thesis, University of California
 Gorgas J., Efstathiou G., Salamanca A.A., 1990, *MNRAS*, 245, 217
 Guzmán R., 1993, PhD thesis, University of Durham
 Huchra J., Geller M., Clemens C., Tokarz S., Michel A., 1992, *Bull.C.D.S.*, 41, 31
 Jørgensen I., Franx M., Kjaergaard P., 1995, *MNRAS*, 276, 1341
 Jørgensen I., 1997, *MNRAS*, 288, 161
 Lucey J.R., Guzmán R., Steel J., Carter D., 1997, *MNRAS*, 287, 899
 Malumuth E.M., Kriss G.A., Van Dyke Dixon W., Ferguson H.C., Ritchie C., 1992, *AJ*, 104, 495
 McElroy D.B., 1995, *ApJS*, 100, 105
 Saglia R.P., Bertschinger E., Baggley G., Burstein D., Colless M.M., Davies R.L., McMahan R.K., Wegner G., 1993, *MNRAS*, 264, 961
 Saglia R.P., Bertschinger E., Baggley G., Burstein D., Colless

- M.M., Davies R.L., McMahan R.K., Wegner G., 1997, *ApJS*, 109, 79 (Paper IV)
- Saglia R.P., Burstein D., Bertschinger E., Bagglely G., Colless M.M., Davies R.L., McMahan R.K., Wegner G., 1997, *MNRAS*, 292, 499 (Paper III)
- Smith R.J., Lucey J.R., Hudson M.J., Steel J., 1997, *MNRAS*, 291, 461
- Tonry J.L., Davis M., 1979, *AJ*, 84, 1511
- Trager S.C., Worthey G., Faber S.M., Burstein D., González J.J., 1998, *ApJS*, in press
- Tripicco M.J., Bell R.A., 1995, *AJ*, 110, 3035
- Wegner G., Colless M.M., Bagglely G., Davies R.L., Bertschinger E., Burstein D., McMahan R.K., Saglia R.P., 1996, *ApJS*, 106, 1 (Paper I)
- Whitmore B.C., McElroy D.B., Tonry J.L., 1985, *ApJS*, 59, 1
- Worthey G., 1993, PhD thesis, University of California
- Worthey G., Faber S.M., González J.J., Burstein D., 1994, *ApJS*, 94, 687
- Zabludoff A.I., Geller M.J., Huchra J.P., Vogeley M.S., 1993, *AJ*, 106, 1273

APPENDIX A: OBSERVING DETAILS

This appendix gives further details of the instrumental configurations used on different telescopes.

MDM 2.4m: The Mark IIIa spectrograph, with a 1.87 arcsec wide slit, was used for all runs up to the end of 1988; from 1989 this was replaced by the Mark IIIb spectrograph, which is identical except that a 1.68 arcsec slit was used (except for run 113, when the slit width was 2.36 arcsec). For runs 101–103 a 600 lines/mm grism blazed at 4600Å was used; for all subsequent runs, a 600 lines/mm grism blazed at 5700Å was employed. The slit was usually oriented N–S. Two-pixel binning perpendicular to the dispersion direction was employed to lower the readout noise.

KPNO 4m: The RC spectrograph and grating KPC-17B (527 lines/mm) were used with the UV Fast Camera and the TI2 CCD.

KPNO 2.1m: The Gold spectrograph/camera and grating #240 (500 lines/mm) were used with the TI5 CCD.

WHT 4.2m: The blue arm of the ISIS spectrograph was used with the CCD-IPCS imaging photon counting system. Most objects were observed using the R600B grating (600 lines/mm), but one object (J26 A, GIN=648) was observed with the R300B grating (300 lines/mm).

INT 2.5m: The Intermediate Dispersion Spectrograph (IDS) and R632V grating (632 lines/mm) were used with the 235mm camera for all runs.

SSO 2.3m: Both runs used the blue arm of the Double Beam Spectrograph (DBS) with a 600 lines/mm grating. Run 130 used the Photon Counting Array (PCA), while run 132 used a Loral CCD.

MMT Blue: The ‘Big Blue’ spectrograph was employed with a 300 lines/mm grating (blazed at 4800Å in first order) and the Reticon detector. The MMT image stacker gave two 2.5 arcsec circular apertures separated by 36 arcsec.

MMT Red: The MMT Red Channel was used with a 600 lines/mm grating (blazed at 4800Å) and the 800×800 TI CCD binned by two pixels perpendicular to the dispersion. The slit was 1.5×180 arcsec, but heavily vignetted in the outer 30 arcsec in one direction.

Calar Alto 2.2m: The Cassegrain Boller & Chivens slit

spectrograph with grating #7 (60 Å/mm) was used in combination with the TEK#6 CCD.

ESO 3.6m: The MEFOS fibre feed and the Boller & Chivens spectrograph were used. MEFOS has 58 2.6 arcsec diameter fibres (29 for targets and 29 for sky) positioned within a 1 degree diameter field at prime focus. The detector was a Tektronix TK512CB CCD (ESO#32).

CTIO 4m: The ARGUS 24-object fibre spectrograph was used. ARGUS has a 50 arcmin field at the f/2.8 prime focus. Each of the 24 arms holds two 1.9 arcsec diameter fibres which lie 36 arcsec apart on the sky; one arm is positioned on the target and the other on sky. The fibres feed a thermally and mechanically isolated bench spectrograph with a 510mm focal length Schmidt blue collimator and a 229mm focal length Schmidt camera. A Reticon II 1200×400 CCD detector was used with grating KPGL #3.